Naval Research Laboratory

Washington, DC 20375-5320

NRL/MR/6180--03-8700

Pyrolysis and Boundary Layer Combustion of a Non-Charring Solid Plate Under Forced Flow

RAMAGOPAL ANANTH
PATRICIA A. TATEM

Navy Technology Center for Safety and Survivability
Chemistry Division

CHUKA C. NDUBIZU

Geo-Centers, Inc.
Lanham, MD

July 31, 2003

BEST AVAILABLE COPY

20030826 033

Approved for public release; distribution is unlimited.

REPORT DOCUMENTATION PAGE

Form Approved
OMB No. 0704-0188

Public reporting burden for this collection of information is estimated to average 1 hour per response, including the time for reviewing instructions, searching existing data sources, gathering and maintaining the data needed, and completing and reviewing this collection of information. Send comments regarding this burden estimate or any other aspect of this collection of information, including suggestions for reducing this burden to Department of Defense, Washington Headquarters Services, Directorate for Information Operations and Reports (0704-0188), 1215 Jefferson Davis Highway, Suite 1204, Arlington, VA 22202-4302. Respondents should be aware that notwithstanding any other provision of law, no person shall be subject to any penalty for failing to comply with a collection of information if it does not display a currently valid OMB control number. **PLEASE DO NOT RETURN YOUR FORM TO THE ABOVE ADDRESS.**

1. REPORT DATE *(DD-MM-YYYY)*
July 31, 2003

2. REPORT TYPE
Memorandum report

3. DATES COVERED *(From - To)*

4. TITLE AND SUBTITLE

Pyrolysis and Boundary Layer Combustion of a Non-Charring Solid Plate Under Forced Flow

5a. CONTRACT NUMBER

5b. GRANT NUMBER

5c. PROGRAM ELEMENT NUMBER
62123

6. AUTHOR(S)

Ramagopal Ananth, Patricia A. Tatem, and Chuka C. Ndubizu*

5d. PROJECT NUMBER

5e. TASK NUMBER

5f. WORK UNIT NUMBER
6001

7. PERFORMING ORGANIZATION NAME(S) AND ADDRESS(ES)

Naval Research Laboratory
4555 Overlook Avenue, SW
Washington, DC 20375-5320

8. PERFORMING ORGANIZATION REPORT NUMBER

NRL/MR/6180--03-8700

9. SPONSORING / MONITORING AGENCY NAME(S) AND ADDRESS(ES)

Office of Naval Research
800 North Quincy Street
Arlington, VA 22217

10. SPONSOR / MONITOR'S ACRONYM(S)

11. SPONSOR / MONITOR'S REPORT NUMBER(S)

12. DISTRIBUTION / AVAILABILITY STATEMENT

Approved for public release; distribution is unlimited.

13. SUPPLEMENTARY NOTES

*Geo-Centers, Inc., Lanham, MD

14. ABSTRACT

Solutions of Navier-Stokes (NS) equations were obtained for burning rate Nu and temperature distributions for a flat PMMA plate using an iterative method to impose steady-state, pyrolysis kinetics at the surface. The NS solutions show that Nu depends on two parameters—Reynolds number (Re) and air velocity—unlike the classical solutions, which include the boundary layer approximations. The NS solutions are compared with experiments to show that the curvature and in-depth heat transfer/pyrolysis effects are significant within the pyrolysis zone at large and small burn times, respectively.

15. SUBJECT TERMS

Moving boundary; Flame spread; Solid combustion; Boundary layer

16. SECURITY CLASSIFICATION OF:			17. LIMITATION OF ABSTRACT	18. NUMBER OF PAGES	19a. NAME OF RESPONSIBLE PERSON
a. REPORT	b. ABSTRACT	c. THIS PAGE			Ramagopal Ananth
Unclassified	Unclassified	Unclassified	UL	45	19b. TELEPHONE NUMBER *(include area code)* (202) 767-3197

Standard Form 298 (Rev. 8-98)
Prescribed by ANSI Std. Z39.18

CONTENTS

1.0	INTRODUCTION	1
2.0	APPROACH	3
2.1	Theoretical	3
2.2	Numerical	8
2.3	Emmons Boundary Layer Theory	10
2.4	Experimental	11
3.0	RESULTS AND DISCUSSION	13
3.1	NS for Distributions Along the Solid Surface	15
3.2	Comparision of NS with PMMA Experiments for Flame Temperature	17
3.3	Comparision of NS with Emmons Theory for Burning Rates	20
3.4	Comparision of NS with PMMA Experiments for Burning Rates	22
3.5	Moving Boundary Effects	23
3.6	In-Depth Pyrolysis	24
3.7	Comparisions of NS with Literature Data	25
4.0	CONCLUSIONS	27
5.0	ACKNOWLEDGMENTS	27
6.0	REFERENCES	28
APPENDIX A- CONSERVATION EQUATIONS		A-1
A.1	Transport Fluxes	A-2
A.2	Thermodynamic Equations of State	A-4

A.3 **Transport Properties** A-4

A.4 **Radiative Loss** A-6

A.5 **Boundary Conditions** A-6

A5.1 **At inlet, x=0 and all y values** A-6

A5.2 **At outlet, x=L and all y values** A-7

A5.3 **On top solid wall and non-fuel sections 1 and 3 of the bottom wall y=H,y=0** A-7

A5.4 **At impermeable sections of the bottom wall, y=0** A-8

A.6 **Initial conditions** A-8

NOMENCLATURE

Text

A	Coefficient in Arrhenius rate expression, $(\#molecules/cm^3)^{-(m+n-1)}\ sec^{-1}$
Av	Avgadro number, #molecules/gmole
$a1_k.a4_k$	Fitted coefficients in polynomial expression for specific enthalpy, h_k, of specie k
B	Spaulding's mass transfer number (B=1.3 for PMMA)
$b1_{kl}$	Fitted coefficients in power law expression for diffusivity, D_{kl}, of a binary mixture containing species k and l
$b2_{kl}$	Fitted coefficients in power law expression for diffusivity, D_{kl}, of a binary mixture containing species k and l
C_k	Number density of the specie, k, #molecules/cm^3
$c1_k$	Fitted coefficients in power law expression for viscosity, μ_k, of specie k
$c2_k$	Fitted coefficients in power law expression for viscosity, μ_k, of specie k
D_{kl}	Diffusion coefficient of specie k in a binary mixture of species k and l, cm^2/sec
D_{km}	Diffusivity of specie k in a gas mixture, cm^2/sec
Da	Damkohler number, $k_p x_l/U$
$d1_k$	Fitted coefficients in power law expression for thermal conductivity, λ_k, of specie k
$d2_k$	Fitted coefficients in power law expression for thermal conductivity, λ_k, of specie k
E	Total energy density of gas mixture, ergs/cm^3
E_a	Reaction activation energy, ergs/gmole
e	Specific energy of gas mixture, ergs/gm
f	Similarity function in the classical boundary layer solution, f(0)=-0.3 for PMMA
Gr	Grashof number
H	Height of the channel, cm
HRR_v	Energy release rate per unit volume, ergs/cm^3sec
h_k	Specific enthalpy of specie k, ergs/gmole
h	Surface heat transfer coefficient, ergs/cm^2.sec.K
K_k	Fitted coefficients in polynomial expression for radiation extinction coefficient of specie k
K_{pk}	Gray body radiation extinction coefficient of specie k=CO_2, H_2O
K_{pm}	Gray body radiation extinction coefficient of gas mixture
k_c	Second–order kinetic constant for combustion, cm^3/gmole.sec

k_p	Pseudo first-order kinetic constant for combustion, $k_c C_{O2}$, sec^{-1}
L	Total length of the plate, $L=L_1+L_2+L_3$, cm
$L_{1,2,3}$	Lengths of the leading non-porous section 1, porous plate section 2, and post-flame,non-porous section 3 respectively, cm
Le	Lewis number
M_k	Molecular weight of specie k, gm/gmole
$\dot{m}$	Pyrolysis rate of PMMA, gm/cm^2sec
Nu	Nusselt number
NS	Navier-Stokes
P	Pressure, $dynes/cm^2$
Pr	Prandtl number
Q_p	Heat of PMMA pyrolysis, $1.6x10^{10}$ ergs/gm
Q_r	Radiative heat loss from the gas phase, $ergs/cm^3sec$
q_i	Heat flux in direction i, $ergs/cm^2sec$
q_w	Heat flux at the solid surface, $ergs/cm^2sec$
R	Universal gas constant, $8.3144x10^7$ ergs/gmole.K
Re	Reynolds number, $Re=Ux_l/\nu$, where ν =0.157 cm^2/sec is used for the kinematic viscosity of the bulk air
r_0	PMMA surface regression rate, cm/sec
Sc	Schmidt number
T	Temperature, K
t	Time, sec
U	Free stream air velocity, cm/sec
U_{dk}	Diffusion velocity for specie k in x-direction, cm/sec
u	Axial gas velocity in x-direction, cm/sec
V_{dk}	Diffusion velocity for specie k in y-direction, cm/sec
V_w	Gas ejection velocity from the PMMA surface, cm/sec
v	Vertical gas velocity in y-direction, cm/sec
W_k	Rate of consumption or production of specie k due to reaction, $\#molecules/cm^3sec$
X_k	Mole fraction of specie k
x	Axial distance from the leading edge of the leading non-porous section, cm
x_l	Axial distance from the leading edge of the PMMA plate, x_l=x-1.7 c

Y_k	Mass fraction of specie k
y	Vertical distance from the solid surface, cm

Greek Symbols

δ	Flame standoff distance; distance between flame (peak temperature) and PMMA surface, cm
ΔH_c	Heat of combustion, 2.53×10^{10} ergs/gmole
ΔT	Constant reference temperature difference between the flame and PMMA surface, 1200 K
ε	Intercept for linear representation of NS solutions for Nu vs $Re^{1/2}$ at large values of Re
τ_{ij}	Stress tensor, dynes/cm^2
λ_k	Thermal conductivity of specie k, ergs/cm.sec.K
λ_m	Thermal conductivity of gas mixture, ergs/cm.sec.K
λ_w	Constant reference thermal conductivity at surface (air at 700K), 0.052 W/mK
μ_k	Dynamic viscosity of specie k, gm/cm-sec
μ_m	Dynamic viscosity of gas mixture, gm/cm-sec
ν	Kinematic viscosity of gas mixture, cm^2/sec
ρ	gas density, gm/cm^3
ρ_s	Constant PMMA density, 1.19 gm/cm^3
ϕ_{kj}	Dimensionless mixture property in the expression for mixture viscosity, μ_m

Subscripts

c	Combustion
d	Diffusion
i	Index in x-direction, i=1,...,nx
j	Index in y-direction, j=1,..., ny
k	Specie index, k=1,.., 5
l	Specie index, l=1,.., 5
m	gas mixture
p	Gray body radiation
r	Radiation
w,s	At the surface of the plate
0,∞	At the inlet or in the bulk of the air

Pyrolysis and Boundary Layer Combustion of a Non-Charring Solid Plate Under Forced Flow

1.0 INTRODUCTION

Burning rate is a measure of flammability of a material and is a critical parameter in fire threat evaluation and for designing fire-fighting systems. Burning vertical walls and ceilings often form boundary layer flames in practice in which burning rates play a fundamental role in determining flame size and flame spread [1]. To gain insights, theoretical and laboratory studies often employ well controlled forced convection, instead of the natural convection, and form non-spreading boundary layer flames on a non-charring polymer plate, which has well defined physical properties (e.g., polymethyl methacrylate, PMMA) [2]. In the boundary layer configuration, gas phase transport and heat flux from the flame to the surface decrease significantly with distance along the fuel surface as the boundary layer thickness increases. The heat feedback drives the pyrolytic reactions and in-depth heat and mass transfer in the condensed phase. Due to the large thermal mass of the condensed phase, transport occurs at a slow rate involving a long transient unlike the transport in the gas phase [3]. Furthermore, the heat flux may also depend on the shape of the surface, which may change significantly with time within the pyrolysis zone. Therefore, the pyrolysis or burning rates vary with distance along the surface as well as the burn time and are not clearly understood. Also, the classical boundary layer flame approximations may not be accurate within the pyrolysis zone, which may not extend to a large enough distance from the leading edge due to the long transient created by the small values of the surface heat flux.

Emmons [4] obtained similarity solutions of Navier-Stokes (NS) equations by making classical boundary layer approximations, which consist of infinite rate kinetics, unit Lewis Le, Prandtl Pr and Schmidt Sc numbers, constant surface temperature and composition. He obtained an analytical expression that showed that the local burning rate or mass loss rate $\dot{m}$ varies inversely with the square-root of distance from the leading edge x_l and directly with the square-root of the air velocity U. Therefore, the dimensionless regression rate or Nusselt number Nu is proportional to $Re^{1/2}$, where Re is the Reynolds number. Due to the simplicity of the closed form equation, the Emmons classical solutions have been used widely and provide a fundamental basis for understanding combustion of liquid and solid fuels. Sibulkin et al. [5] obtained similar solutions for buoyancy-driven flow instead of forced flow considered by Emmons [4], but included the effects of finite rate combustion kinetics. Chen and Tien [6] obtained numerical solutions of NS equations at a small neighborhood (few mm @ U=100 cm/sec) near the leading edge of a forced convection boundary layer flame without some of the boundary layer approximations. However, the solutions focused on flame attachment at small values of the Reynolds number, $Re=Ux_l/\nu < 10$, rather than the burning rate distributions. Their solutions showed the effect of decreasing Damkohler number Da on flame transition from a "closed" to an "open" flame. Mao, Kodama, and Fernandez-Pello [7] presented NS solutions for mixed

Manuscript approved June 17, 2003.

convection effects on thermal, concentration and velocity fields in a boundary layer flame rather than the burning rate distributions. Kodama, Miyasaka and Fernandez-Pello [8] calculated the effects of air flow velocity and oxygen mass fraction on extinction distance for the mixed convection boundary layer flame modeled by Mao et al. [7]. They compared the predicted extinction lengths with those measured from diffusion flames formed by injecting heptane through a porous plate burner. In this work, we obtain solutions of steady-state NS equations, which are similar to those considered by Mao et al. but include the effects of composition-dependent properties and surface-pyrolysis kinetics, which is imposed by developing a multi-variable iterative method. Our first goal is to predict the burning rate profiles along the fuel surface without the boundary layer approximations and make quantitative comparisons with the classical Emmons solutions.

PMMA forms a thin layer of melt, which unzips almost entirely to the monomer (methyl methacrylate) by a stepwise mechanism [9]. The monomer rapidly vaporizes and escapes from the superheated polymer melt. Therefore, PMMA pyrolysis has been commonly viewed as a surface process leading to quasi-steady-state burning. In the boundary layer configuration, however, the heat flux from the flame to the surface is low at large distances from the leading edge. At the low surface heat flux, the thermal boundary layer thickness in the condensed phase is significant and the pyrolysis can occur in-depth. Also, the heat-up time is large at low surface heat flux due to the large thermal mass of the condensed phase. Experiments [10,11] on PMMA plate exposed to uniform, pre-specified, radiant flux clearly showed that the heat transfer into the condensed phase occurs slowly due to the large thermal mass and phase change phenomena. In these experiments, which were performed without combustion, the rate of in-depth pyrolysis increased with time before reaching a steady state. Furthermore, the time to obtain a steady rate increased significantly as the radiant heat flux decreased.

Mekki et al. [12] performed experiments on wind-aided flame spread underneath a PMMA plate, which was fixed to the ceiling of a rectangular channel. Mekki et al. measured the total specie production rate and inferred that the total pyrolysis rate increased with time. They also found that the total specie production rate increased linearly with the length of the pyrolysis zone contrary to the square-root relationship predicted by the Emmons theory. Agrawal and Atreya [3] generalized Emmons solutions by combining it with a one-dimensional theory for the transient heat up and pyrolysis of a PMMA plate. Agrawal and Atreya [3] showed qualitative agreement between their theory and the measurements of Mekki et al [12] for the total production rate of species. However, very few studies focused directly on the burning rate distributions and the role of transient pyrolysis, which remains unclear for a forced-flow boundary layer flame.

Zhou and Fernandez-Pello [13] measured local regression rate distributions for wind-aided flame spread over a PMMA plate at a large (>15 cm) distance from the leading edge. The flame spread experiments were conducted both without and with externally imposed turbulence on the bulk flow. The dimensionless regression rates Nu were found to be proportional to $Re^{1/2}$ for laminar flow in qualitative agreement with Emmons solutions at large distances (15 cm $<x_1<$ 70 cm) from the leading edge. Their results also seem to be consistent with the data discussed by Ahmed and Faeth [14] for buoyancy-driven flames formed over a vertical plate. Agrawal [15] performed experiments using an apparatus similar to the one used by Mekki et al. [12] for flame

spread underneath a PMMA surface. Agrawal [15] measured the regression rates for distances ($0 < x_l < 40$ cm) from the leading edge. At large values of x_l, the heat flux arriving at the surface is small, and one might expect a significant in-depth pyrolysis and a long transient for heat-up of the cold PMMA plate. Therefore, Agrawal [15] attempted to account for the unsteady transport in the condensed phase using the theory of Agrawal and Atreya [3] and reported the surface heat flux profiles q_w, which are time independent. Near the leading edge of the plate, the qw profile exhibited a peak. The flux increased within the first 3 cm from the leading edge of the plate and decreased with the increased axial distance x_l. The steady-state surface flux was found to decrease as $x_l^{-0.8}$ rather than $x_l^{-0.5}$ predicted by Emmons at large values of x_l. Unlike the flame spread experiments, Krishnamurty and Williams [2] established quickly (5 sec) a forced-flow boundary layer flame by igniting the entire surface of a PMMA plate and reported regression rates for different concentrations of oxygen in the bulk flow of the oxidizer. The regression rates were measured for a fixed, short burn time (t~100 sec) at three positions along the length (15 cm) of the plate. The data were found to be in good agreement with Emmons solutions for high oxygen concentration. At ambient air, however, the measured regression rates were found to be significantly lower than the predictions of the classical theory. The exact reasons for these discrepancies among the data and the classical theory have not been clear.

Emmons solutions and the NS solutions presented here assume that the fuel surface remains flat as it burns at a steady rate. However, the surface heat flux and the local regression rates are non-uniform along the PMMA plate. Therefore, the surface regresses non-uniformly and an initially flat surface of a real material, such as PMMA, develops curvature as the time progresses. Indeed, experiments [16,17] performed in our laboratory have recently shown that the surface curvature affects local heat, mass and momentum transport, which in turn can have significant effect on the local burning rates for PMMA. Furthermore, Hegab et al. [18] have recently obtained self-consistent solutions to describe burning of a sandwich propellant exposed to quiescent air and showed significant moving boundary effects on the burning rates.

Therefore, our second objective is to make quantitative comparisons of the steady-state NS solutions, and Emmons solutions with our experimental measurements of regression rate distributions [16,17] at different burn times (5 to 20 min) to study the transient effects and the validity of the approximations (flat surface and steady surface-pyrolysis). The experiments were performed on non-spreading, forced-flow, boundary layer flames, which were formed quickly by exposing the entire surface of a PMMA plate (10 cm) to uniform radiant flux rather than allow co-current flame spread. Therefore, every point on the surface was exposed to the flame for a prespecified length of time, which was varied systematically in the experiments until steady-state is approached.

2.0 APPROACH

Our approach includes both numerical modeling and laboratory experiments. We will focus here mainly on the theoretical aspects of the problem and provide only a brief description of the experiments. Further details of the experiments can be found in a separate NRL memo report, NRL/MR/6180-02-8630 [17].

2.1 *Theoretical*

We consider laminar flow of air past a flat solid surface, which consists of a leading inert plate (1.7 cm), followed by a PMMA plate (6.7 cm), followed by another inert plate (8 cm) as shown in Fig 1. The leading plate establishes the no-slip condition and a Blassius momentum

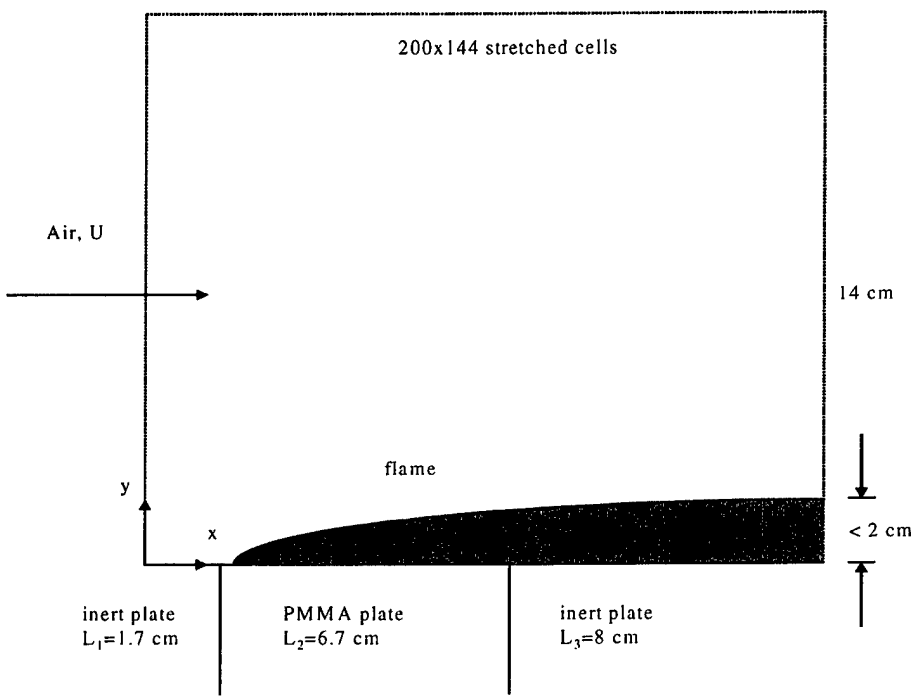

Figure 1 Boundary Layer Flame Formed Over a PMMA Plate

boundary layer. The lengths of the inert plates were chosen to minimize the effects of in-flow and out-flow boundary conditions on the combustion region. The width of the plate is assumed to be infinite. The air enters the domain at a uniform velocity parallel to the plate and forms a boundary layer over the surface. The nominal Reynolds number, $Re=Ux_l/\nu$ is 7000 (laminar) or less, where x_l is the distance from the leading edge of the fuel plate, x_l=x-1.7, where x is

measured from the leading edge of the inert plate. The nominal value of Re is evaluated using the ambient value of the kinematic viscosity, ν=0.157 cm^2/sec. Mao et al. [19] showed that the effects of buoyancy and forced flow on combustion scale as $Gr/Re^{2.5}$ for a horizontal fuel surface rather than the commonly used relationship Gr/Re^2 for a vertical surface. A small difference in the exponent of Re has a large effect on the ratio and on the significance of buoyancy effects. Therefore, for the small sample length (<10 cm) and for U>60 cm/sec, $Gr/Re^{2.5}$ <0.18 and the forced convection are assumed to dominate the gravity effects.

Initially, the air and the surface are kept at room temperature, and the entire fuel surface is ignited by adding external energy to the gases above the plate for a short period of time. Upon ignition, the PMMA undergoes pyrolysis to form monomer vapor, which mixes with the air by convection and diffusion. The fuel-air mixture undergoes combustion and a boundary layer flame is established above the fuel plate. The unsteady, full NS equations describe the development of the flame from ignition to steady state. The coordinates x and y are fixed to the leading edge of the leading inert plate and represent distances along the surface and perpendicular to the surface, respectively. The conservation equations are given in Appendix A.

Combustion of the methyl methacrylate monomer is assumed to take place in a single step to produce stochiometric amounts of carbon dioxide and water according to

$$C_5H_8O_2 + 6O_2 = 5CO_2 + 4H_2O\,. \qquad (1)$$

Therefore, the production rates of CO_2 and H_2O and consumption rates of O_2 are proportional to the rate of combustion of fuel W_k, which is assumed to follow second order reaction kinetics given by Seshadri and Williams [20].

$$W_k = k_c C_k C_{O2}\,, \qquad (2)$$

where k_c is the kinetic constant in cm^3/gmole-sec. It is given by

$$k_c = 2.3x10^{16}\exp(-43000/RT)\,, \qquad (3)$$

where T and R are the gas temperature and the gas constant, respectively. The energy release rate per unit volume HRR_v is given by

$$HRR_v = \Delta H_c W_k / Av\,, \qquad (4)$$

where ΔH_c (2530 KJ/gmole) and Av are the heat of combustion and Avogadro number, respectively.

Binary diffusion coefficients D_{kl}, viscosity μ_{kl} and conductivity λ_{kl} are calculated for each specie from power law correlation of Chapman-Enskog equations as functions of temperature as shown in Appendix A The mole fraction of fuel vapor in the combustion gases is typically much smaller than 1.0. The properties of n-pentane gas are used for the pure monomer vapor after

correcting for the molecular weight difference, which is about 30%. Specific heats of pure species are taken from standard tables. The properties of gas mixture are evaluated from the pure specie values using the mixture rules described in Appendix A

As the heat from the flame is transferred to the polymer surface, the polymer first softens and begins to melt around 100 ^{0}C [9]. Upon further heating, the melt begins to pyrolyze around 250 ^{0}C and unzips to form the monomer. Therefore, the monomer, which has a normal boiling point of about 101 ^{0}C, instantly evaporates from the super-heated polymer melt and forms bubbles, which are ejected to the surface. As a result the melt is mostly composed of the polymer and is very viscous. The thickness of the melt layer depends on the heat flux to the surface. At high surface heat flux, which occurs near the flame attachment point, the melt layer is barely visible due to high temperature gradients, and the pyrolysis reaction may be assumed to occur at the surface. However, as x_l increases and qw decreases, the melt layer becomes thick due to small temperature gradients, and pyrolysis may occur in depth at an unsteady rate. However, due to the small length of the PMMA plate considered in this analysis, we assume that the melt layer is very thin and the pyrolysis reaction occurs essentially at the solid surface at a steady rate following an ablative step;

$$[(-C_5H_8O_2-)_n]_{solid} \rightarrow n[C_5H_8O_2]_{vapor}. \qquad (5)$$

The rate of pyrolysis is determined both by the rate of heat transfer to the polymer and the intrinsic kinetics of the pyrolysis reaction. Therefore, in the limit of infinite heat transfer, the pyrolysis rate is determined by the intrinsic chemical kinetics of the pyrolysis, which are measured under isothermal conditions to eliminate resistance to heat transport. On the other hand, in the limit of infinite rate chemical kinetics, the pyrolysis rate is determined by the rate of heat transfer to the polymer. We assume that the intrinsic chemical kinetics follows a zeroth order kinetic expression given by Arisawa and Brill [21]. Arisawa and Brill [21] performed experiments with very thin films of anionically polymerized, high-molecular-weight (131,000) PMMA at different values of the preset temperature T_s (653-733 K). The temperature was kept uniform (+/- 2 ^{0}K) across the film in their experiments by supplying heat to compensate for the cooling due to endothermic pyrolysis. Therefore, they provide intrinsic measurements of the kinetics that depend only on the temperature, which was calibrated against compounds with standard melting points. The temperature is kept uniform across the film in their experiments and, therefore, provide intrinsic measurements of the kinetics that depend only on the temperature and independent of heat transfer limitations. Their rate constants, which are in 1/sec, were multiplied by the thickness (83 μm) of the film and the polymer density (ρ_s=1.19 gm/cm^3) to obtain an expression for the surface mass flux or the pyrolysis rate, $\dot{m}$ in gm/cm^{2}sec, which is given by

$$r_0\rho_s = \dot{m} = 8x10^{17}\exp(-66000/RT_s)\ . \qquad (6)$$

Equation (6) shows an exponential relationship between the pyrolysis rate and the surface temperature, which varies along the surface. Therefore, an order of magnitude change in the pyrolysis rate results in a small change of 35 K in surface temperature due to the high activation energy (66 Kcal/gmole or 2.76 x10^5 KJ/Kgmole). Here, r_0 is the local regression rate of the surface. Significantly lower values than 66 Kcal/gmol for E_a were reported by others [2,10]. Kashiwagi et al. [22] showed that the activation energy is generally much larger (56 Kcal/gmole) in the absence of oxygen at the PMMA surface than that (15 Kcal/gmole) for oxidative degradation. Our simulations show very little oxygen concentration on the PMMA surface and also r_0 to be less sensitive to E_a as discussed later.

At the PMMA surface, the pyrolysis rate must equal the sum of convective and diffusive fluxes for the monomer vapor and is stated by

$$\dot{m} = \dot{m} X_k(t,x,0) - D_{km}\rho dX_k(t,x,0)/dy. \qquad (7)$$

The net flux for oxygen, nitrogen, carbon dioxide and water vapor at the surface is zero and is given by

$$\dot{m} X_k(t,x,0) - D_{km}\rho dX_k(t,x,0)/dy = 0, \qquad (8)$$

where X_k is the mole fraction of the specie k. As the boundary layer thickness increases along the plate, both the diffusive flux and $\dot{m}$ decrease. Therefore, equation (8) requires that X_k vary along the surface. The heat transfer from the flame to the surface should equal the heat needed to pyrolyze the solid and is given by

$$\dot{m} Q_p = \lambda_m dT(t,x,0)/dy. \qquad (9)$$

Here, Q_p (1.62x10^3 KJ/Kg) is the endothermic heat of pyrolysis for PMMA. In writing equation (9), net radiative heat feedback is neglected compared to the gas phase heat transfer by conduction and convection for the small length of the PMMA plate considered in this analysis. The net radiation is the result of radiative heat feedback to the surface and re-radiative cooling from the surface, which may be comparable due to high emissivity of black PMMA surface [2]. The in-depth heat transfer and pyrolysis are expected to become significant at increasing distances from the leading edge of the plate as discussed later, and equation (9) becomes less accurate. In-depth heat transfer is also assumed to be small for the small length of the plate considered in this study. The velocity components at the PMMA surface are given by

$$V_w = \frac{\dot{m}}{\rho(t,x,0)}, u(t,x,0) = 0 . \qquad (10a, b)$$

The dimensionless regression rate Nu is defined as

$$Nu = \frac{hx_l}{\lambda_w} = \frac{r_0 \rho_s Q_p x_l}{\lambda_w \Delta T}, \quad (11)$$

where the thermal conductivity of gas at the PMMA surface λ_w=0.00052W/m^{2}K is taken as the value for air at 700 ^{0}K. Also, the temperature drop across the flame ΔT=1200 ^{0}K was used since it did not change significantly with x for the relatively small length (<10 cm) of the fuel plate considered in this study.

At low air velocities, the flame attaches close to the leading edge of the PMMA plate. Therefore, the heat transfer characteristics of the leading plate in front of the sample could play a role in the attachment dynamics. Therefore, heat loss through the leading plate is assumed to follow Newton's law of cooling with a characteristic heat transfer coefficient (h=173 W/m^{2}K). No-slip condition was applied along the entire surface. The no-slip was applied only on a small portion of the leading plate to accurately represent the experimental conditions. The post-flame plate temperature is kept uniform at the trailing edge temperature of the PMMA plate. At the top of the computational domain, air is allowed to flow axially with slip. The boundary conditions for the inert plates, inlet and outlet are also given in Appendix A.

Due to high thermal mass of the condensed phases, the pyrolysis and transport phenomena occur at a very slow rate, unlike the phenomena in the gas phase. Therefore, the surface is assumed to remain flat despite non-uniform heat feedback and regression of the surface. The flat plate assumption, together with the surface-pyrolysis assumption leads to quasi-steady-state in which all of the dependent variables in the conservation equations and the burning rate distributions become independent of time at a short time (< 2 sec) after the ignition. Therefore, equations (6-10) are applied at y=0. The implications of these assumptions on the comparison between the steady-state NS solutions and the experiments will be discussed later.

2.2 Numerical

There are several unknowns, i.e., ρ, u, v, P, E, and C_k in the gas phase, as well as temperature, specie concentrations, and vertical velocity distributions along the surface of the PMMA plate. All of these are calculated as functions of position x and y and time t. One typically specifies inlet velocity u_0, density ρ_0, composition C_{k0}, and temperature T_0 (or energy E_0) of the air. The equations are discretized by a finite volume method on an Eularian domain containing about 192x144 finite volume cells in x and y directions, respectively. The cells are clustered closely near the leading edge of the flame, which is not known a priori. At large velocities, the flame attaches downstream and the cell placement is corrected accordingly. The minimum cell size inside the flame is 0.2 mm x 0.2 mm. Therefore, at the very leading edge, as x_l becomes comparable to 0.2 mm, the solutions presented here become less accurate. The cells are stretched in both directions from the leading edge. The convective, diffusive, combustion and radiation contributions are solved by separate algorithms using separate time steps, which are

typically either smaller or equal to the global time step. Diffusion and reaction processes are subcycled within a global time step and cumulative contributions from each process are calculated. These terms are then coupled together by time-step splitting as discussed by Oran and Boris [23]. The global time step is chosen such that the diffusion processes are not subcycled by more than three times. The global time step is typically of the order of 10 and 50 msec during and after ignition, respectively.

Ignition along the entire length of the plate was achieved by adding external energy to several number of rows of cells above the plate for about msec. During the ignition time, the PMMA surface temperature was prespecified at 700 K to ensure that the fuel vapor is ejected continuously from the surface forming combustible mixture above the plate. Therefore, it simulates qualitatively the radiative ignition employed in the experiments, which are discussed later. The magnitudes of ignition time scales are much smaller in the numerical simulations than those employed in the experiments. Therefore, the transient behavior is expected to differ between the simulations and the experiments for the gas phase. However, the ignition method has little effect on the steady state results for the gas phase, which is the main focus of the computations.

Convection equations are solved by the high-order implicit algorithm, Barely Implicit Correction to Flux-Corrected Transport (BIC-FCT), which was developed by Patnaik et al.[24] to solve the convection part of the equations for slow flows. The Flux-Corrected Transport (FCT) is an explicit scheme for the solution of hyperbolic equations. Therefore, it requires very small time steps dictated by sound speed following Courant-Friedrichs-Lewy condition. BIC-FCT was developed based on the suggestion by Casuli and Greenspan [25] that only the pressure in momentum equation and velocity in energy equations needs to be treated implicitly to increase the time step to that based on fluid velocity rather than the sound speed. This method involves solution of an elliptic equation for pressure which is solved using MGRID algorithm discussed in detail by DeVore [26]. Typically, the courant number based on maximum fluid velocity and minimum cell size is smaller than 0.3.

Diffusion equations are discretized using explicit finite difference approximations. The time steps for the subcycle are calculated based on minimum cell size and maximum diffusivity in the domain. If these time steps are more than one third of the global time step, then the global time step is reduced. At the end of each subcycle, diffusion contributions to specie concentrations, temperature, and momentum are updated for mass, heat and momentum, respectively.

Reaction contribution is described by a single nonlinear stiff ordinary differential equation and is solved by using Burlich-Stoer algorithm with Rhomberg interpolation as described by Press et al. [27]. Unlike the diffusion processes, the reaction time steps are evaluated based on local values of the variables rather than global maximum/minimum values in the domain. The time steps are calculated cell by cell from the local values of rate constant, specie concentrations and temperature and vary widely across the domain. Typically, the time steps can be hundreds of times smaller than the global time step, especially during ignition near the leading edge of the porous plate. After ignition, the time step increases by a factor of 3-10 in

the hottest regions. Therefore, the reaction calculations are subcycled to a varying degree within the domain. Specie concentrations are updated at the end of each subcycle. A very significant cost of computation is incurred in reaction calculations.

Calculation of the burning rates require special attention. Unlike the gas phase, which is treated as a continuum, the PMMA surface is treated as plane of discontinuity on which equations (6-10) are imposed by a multi-variable fixed point iterative method. In this method, at each time step, new values of $\dot{m}$, X_k and T_s are evaluated from equations (6) to (10), in which old values are used to calculate the derivatives. Solution of the pyrolysis equation (6) needs special attention. An implicit form of the pyrolysis equation was derived by substituting equation (6) into (9) and was solved by Newton-Raphson iteration with bisection to obtain the new value of T_s. Therefore, within each fixed-point iteration, only T_s was solved by the Newton-Raphson method (inner iteration), with both $\dot{m}$ and X_k fixed. If the new values of $\dot{m}$, X_k and T_s are not within a prespecified tolerance of the values from previous fixed point (outer) iteration, the Navier-Stokes equations are re-solved with the new values for the boundary conditions at the surface. Thus, $\dot{m}$, X_k and T_s are iterated until convergence is achieved for every cell along the polymer surface, before proceeding to the next time step. The fixed-point iterations are also used to implement the mixed boundary condition, equation (A34), for calculating the surface temperature of the leading plate, without the Newton-Raphson inner iterations. A similar method was implemented by Ananth et al. [28,29] for studying a boundary layer flame formed over a porous plate without the inner Newton-Raphson iterations.

2.3 Emmons Boundary Layer Theory

One may evaluate the accuracy of the BL approximations by comparing the NS solutions with the classical solutions. Emmons recast the steady-state form of the NS equations given in Appendix A, equations (6-10), and derived an analytical solution by using classical boundary layer approximations described by Williams [30]. For large Re, which occur at high velocities or large values of x_l, axial diffusion terms in NS equations become negligible compared to lateral diffusion. Also, assuming Le=Pr=Sc=1and the combustion kinetics occur at infinite rate (flame sheet approximation), the NS equations were reduced to a homogeneous parabolic equation, which was solved for the burning rate using similarity method. In this method, intrinsic kinetics of surface pyrolysis was assumed to occur at infinite rate so that the pyrolysis rate is determined by the heat feedback. Equation (6) was replaced by constant surface temperature boundary condition, which was prespecified. The boundary layer solution is given by

$$r_0\rho_s = \rho_w V_w = \left(\frac{U\mu_\infty\rho_\infty}{2x_l}\right)^{1/2}(-f(0)). \quad (11)$$

Here, subscript w and ∞ represent values at the the solid surface and in the bulk, respectively. The values of f(0) are represented in analytical form by Glassman [31] as shown below

$$-f(0) = \frac{\ln(1+B)}{2.6B^{0.15}} \quad , \qquad (12)$$

where B is the Spaulding's mass transfer number. Equation (11) can be written in dimensionless form as

$$Nu = \frac{hx_l}{\lambda_w} = \frac{r_0 \rho_s Q_p x}{\lambda_w \Delta T} = \frac{\rho_\infty v_\infty Q_p}{\lambda_w \Delta T \sqrt{2}} (-f(0)) \sqrt{\mathrm{Re}} . \qquad (13)$$

For PMMA, the Spalding's mass transfer number B is given by Kanury [32] and Chen and Tien [6] as 1.3, which is substituted into equation (12) to get f(0)= - 0.3. The value of f(0) is slightly smaller than the value (-0.397) given by Krishnamurthy and Williams [2]. Substituting equation (12) into (13), one obtains for the dimensionless regression rate Nu for PMMA (B=1.3)

$$Nu = \frac{hx_l}{\lambda_w} = 0.1\sqrt{\mathrm{Re}} \ . \qquad (14)$$

An expression for the flame-standoff distance δ may be obtained from equation (14) by making linear approximation for the temperature gradient at the surface to obtain

$$\frac{1}{Nu} = \frac{\lambda_w}{hx_l} = \frac{\delta}{x_l} = \frac{10}{\sqrt{\mathrm{Re}}} \ . \qquad (15)$$

Equation (14) shows clearly that Nu depends only on a single parameter Re. It increases with square-root of U and decreases with square-root of x. Therefore, as x approaches zero as one approaches the leading edge, Nu reaches a very high value due to the neglect of axial diffusion terms in the NS equations. Indeed, we will show that the axial diffusion terms remain significant even at significant distances from the leading edge. Furthermore, the infinite rate kinetics approximation in the NS equations leads to flame "attachment" at the leading edge of the PMMA plate independent of U. Full NS equations, however, predict flame "attachment" at some distance from the leading edge, which is affected by the competition between convection and the finite rate combustion kinetics as discussed later.

2.4 Experimental

Experiments were performed on non-spreading boundary layer flame formed over a relatively short length of black PMMA sample (7.5 cm x 9.5 cm x 2.5 cm). The combustion experiments were conducted for different values of the burn time to record the transient effects. Experimental details are given elsewhere [16,17,33-35] and only a brief description is given here

for completeness. The geometry is similar to that shown in Figure 1. A high molecular weight, black PMMA sample was placed in a cup holder, which has extension plates (lips) to minimize the edge effects. Thin quartz plates are placed all around the fuel plate to minimize excess burning of the edges. The sample is placed at the exit of a channel rather than inside the channel to facilitate temperature mapping of the flame. Air was forced out of the channel at a prespecified center velocity. The velocity distributions across the air jet was found to be flat and did not change significantly along the length of the sample. The entire PMMA surface was exposed to a large radiant panel typically for less than 30 sec. The sample surface is melted and pyrolyzed as evidenced by the formation and ejection of bubbles. The fuel vapors are ignited to quickly form a boundary layer flame. During combustion, a thin film of melt is formed at the surface with intense bubbling near the leading edge and relatively slow bubbling far from the leading edge. The bubbles were very small and barely visible near the leading edge and increase in size with x_l. The width of the flame is much larger than the boundary layer thickness so that the flame can be approximated as being two dimensional.

After about 1 min from the time of ignition, five fine thermocouples are brought into the flame to map the temperature profiles across the flame at five different locations x_l along the plate. The thermocouple readings are reported after a radiation correction. The temperatures were recorded at different distances, Y, measured from the initial position of the surface rather than the regressing surface. The sample was allowed to burn for a prespecified amount of time before the flame was extinguished, and the sample was allowed to cool down. The change in the thickness of the plate due to burning was measured with a micrometer at different distances from the leading edge x_l. Regression rate is the change in the thickness of the sample divided by the burn time. The boundary layer formed was smooth except near the sides and near the trailing edge of the sample due to buoyancy effects. Measurements, however, were made well within the smooth region and along the center line of the sample. Some of the experimental results are summarized below [16,17,33-35]:

(1) At the end of ignition, the PMMA surface was flat. As the time progresses, a step was formed near the flame attachment point. The step size increased in depth and width with t. In the valley, the surface to flame distance increased with time as indicated by a single thermocouple measurements.

(2) At a fixed value of the burn time, the regression rate r_0 increased with x_l and reached a maximum near the flame "attachment point" followed by a decrease in r_0 with x_l.

(3) r_0 decreased significantly with burn time t within the valley at short distances from the leading edge x_l. On the other hand, r_0 increased with t at large values of x_l and was often associated with increased activity of bubbling near the trailing section of the sample plate. As U is increased, bubbling activity in the trailing section increased significantly.

(4) At large values of U, the flame attached downstream of the leading edge of the fuel plate where the valley was formed. As the time progressed, the flame spread very slowly toward the leading edge of the plate while the valley got wider in size.

(5) The surface was semi-solid and the melt layer was barely noticeable near the leading edge. The melt layer thickness appeared to increase with x_l. The melt temperature decreased by ~ 45 K along the length of the sample as indicated by pressing a thermocouple onto the surface.

3.0 RESULTS AND DISCUSSION

Once the geometry, the combustion kinetics and the pyrolysis kinetics are specified, one only needs to specify the air velocity to obtain solutions of the governing equations. Solutions describe the temperature, specie mole fraction, velocity and density profiles as functions of x, y and t [36-41]. Also, the values of $\dot{m}$, X_k and T_s along the surface are predicted. Simulations were performed until steady state, which is achieved in less than a second at the air velocities employed in our experiments. However, our goal is to discuss the steady-state values for gas-phase temperature profiles and burning rates, the quantities that were measured in the experiments for relatively short length (6.5 cm) of the PMMA plate.

Figure 2a shows typical temperature contours for inlet air velocity, U, of 60 cm/sec. The combustion reactions occur mostly in the high temperature region, which is represented by one of the dark bands, and is referred to as the "flame" or "combustion zone". Near the leading edge, fresh fuel comes in contact with fresh air and the combustion rates are very high. Downstream, the products dilute the gases and the combustion rates decrease sharply within a short distance from the leading edge as indicated by the heat release rate contour (HRR_v) shown as a dark line labeled "DEDtrxn" for $1x10^9$ ergs/cm^{3}sec in Figure 2a. The rates of heat and mass transfer between the flame and the surface are also large near the leading edge due to steep gradients, and they decrease with distance from the leading edge as the boundary layer thickness increases. Therefore, near the leading edge, the transport and combustion rates are expected to be closely coupled. The competition between convective transport and reaction kinetics is represented by Damkohler number Da= reaction rate/convection rate= $k_p x_l/U$, where $k_p = k_c C_{O2}$ is the psuedo-first-order rate constant. Here, C_{O2} is taken as the ambient concentration of oxygen in the bulk. At small air velocities, Da is high and the gases get heated up within a short distance from the leading edge x_l by the high rates of heat release. Therefore, the flame "attaches" near the leading edge of the plate. As U is increased, Da decreases, and the flame "attaches" at increasing value of x_l as shown in Figure 2b. Figures 2a and 2b also show that the flame temperature in the combustion zone has not decreased significantly along the length of the PMMA plate. Clearly, as U increses, the heat release rate contour (DEDtrxn) increases in length indicating the increased length of the flame.

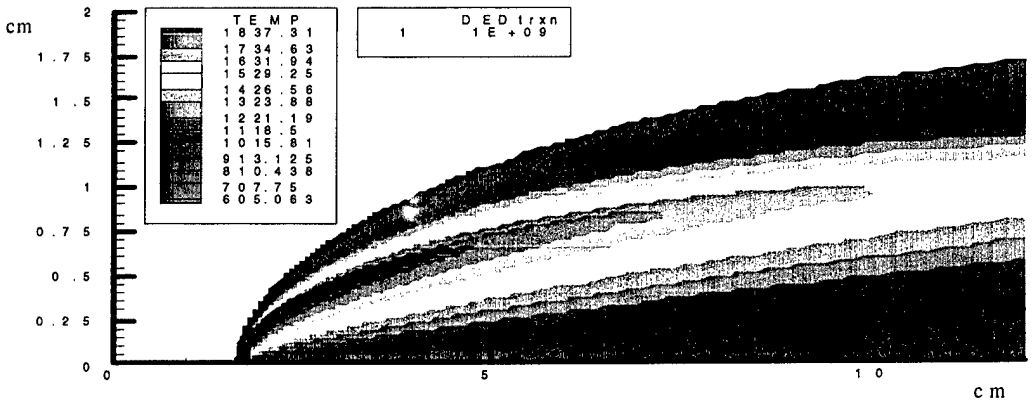

Figure 2a NS Solutions for the Temperature Contours for Boundary Layer Diffusion Flam Over a PMMA Surface at u=60 cm/sec

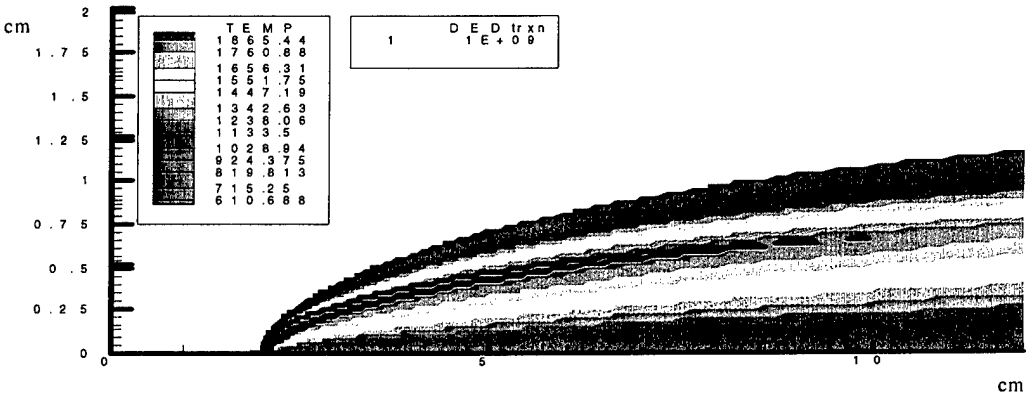

Figure 2b NS Solutions for the Temperature Contours for Boundary Layer Diffusion Flam Over a PMMA Surface at u=169 cm/sec

BEST AVAILABLE COPY

3.1 NS for Distributions Along the Solid Surface

Figure 3 shows the NS solutions for the surface temperature profiles along the length of the sample at different air velocities. As one approaches the flame "attachment" points, shown in Figures 2a and 2b, the surface temperature raises sharply to a maximum and then decreases with x_l as the boundary layer gets thicker reducing the heat feedback. The surface temperature changes by about 40 K over 6.5 cm length of the plate. This is qualitatively consistent with our experiments on PMMA under boundary layer combustion. During combustion, the surface of PMMA appears to be covered with a froth layer consisting of polymer melt and monomer bubbles formed by the unzipping of the polymer. It was observed that the bubbling was intense and bubble size was small near the leading edge. At large values of x_l, the bubbling was slow and bubble size was large. The rate of bubble formation should increase with increased rate of pyrolysis, which occurs at high melt temperature. At high melt temperature, the superheat is higher and the bubble size may be expected to be small. The experiments seem to show that both the bubble size increases and the bubbling rate decreases with x_l. Since the surface is not a well-defined interface between solid and gas phases, it is difficult to measure precisely the temperature changes along the surface. However, we attempted to measure the surface temperature by dipping a fine thermocouple into the froth layer on the surface at different distances from the leading edge x_l. We estimate the temperature drop from x_l=0 to x_l=9 cm is about 40 K, which is comparable to those measured in our experiments and by Vovelle et al. [10] in their experiments on flameless pyrolysis of PMMA. Vovelle et al.[10] measured a change of 30 K as the heat flux changed from 3.0 W/cm^2 to 1.5 W/cm^2. However, the values of T_s and its distribution are determined mainly by the kinetic constants in the pyrolysis kinetics expression given by equation (6). A variation of these constants seem to affect mainly T_s rather than the burning rate distributions. Figure 3 also shows that the increased U moves the flame "attachment" point downstream and the maximum in T_s occurs downstream. Furthermore, increase in U increases T_s slightly at large values of x_l.

The specie concentration profiles along the PMMA surface are shown in Figures 4-6. As Ts decreases along the surface, the rate of formation of MMA decreases as indicated by the decrease in its concentration shown in Figure 4. The mole fraction of MMA in Figure 4 is close to the value of the uniform surface concentration used in the calculations of Mao et al. [7] despite differences in the kinetic constants used between the two studies. Increased U increases MMA concentration as T_s increases. CO_2 concentration increases with x_l as more of the product is produced along the plate and increases with U due to increased production rate as shown in Figure 5. H_2O concentration follows the CO_2 profile. Unlike MMA, CO_2 and H_2O, the oxygen profile is significantly different and is shown in Figure 6. The oxygen concentration drops sharply near the flame attachment point to zero. Therefore, most of the PMMA surface sees only the monomer vapor, products and nitrogen along its surface. This has important implications. Kashiwagi et al. [22] showed that PMMA pyrolysis kinetics is altered by the presence of oxygen

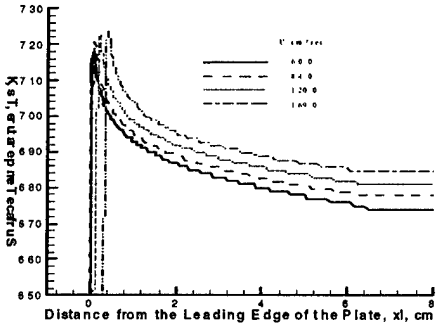

Figure 1 NS Solutions for the Effect of Convection on Surface Temperature Distribution

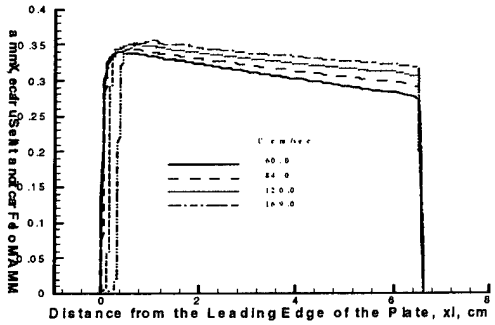

Figure 4 NS Solutions for the Effect of Convection on Monomer Concentration at the Surface

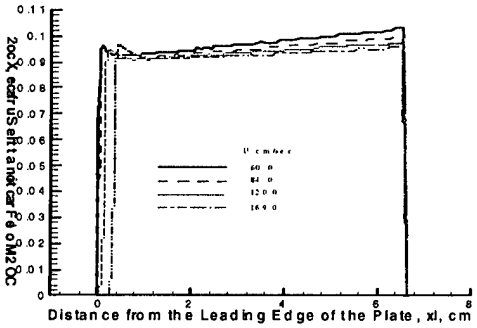

Figure 5 NS solutions for the Effect of Convection on CO_2 concentration at the Surface

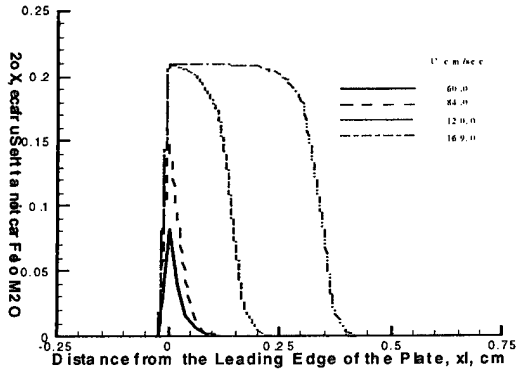

Figure 6 NS Solutions for the Effect of Convection on Oxygen Concentration at the Surface

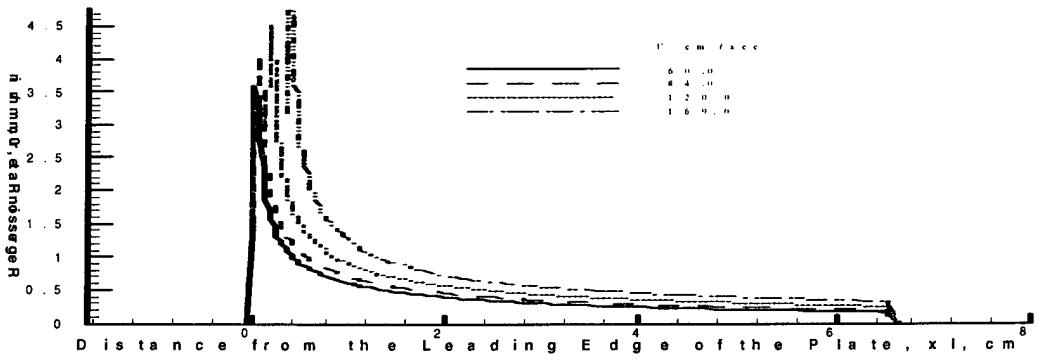

Figure 7 NS Solutions for the Burning Rate Distribution along the Surface and the Effects of Convection

BEST AVAILABLE COPY

in flameless pyrolysis experiments under a radiant panel. The higher the oxygenconcentration the lower the value of E_a for the pyrolysis kinetics, which is attributed to O_2 diffusion into the melt. Our calculations appear to suggest that, under the boundary layer combustion conditions, PMMA pyrolysis occurs without the influence of oxygen at the surface.

The NS solutions for local regression rates r_0 are obtained by dividing the pyrolysis rate $\dot{m}$, which is given by equations (6) to (10), by the polymer density and is plotted in Figure 7 for different air velocities. The regression rate is determined by the combustion kinetics and by the heat transfer from the flame to the surface due to convection and conduction as described by equations (6) to (10). As one might expect, the NS solutions are less accurate at extremely small values of x_l, as they become comparable to the cell size (0.2 mm) used in the computations. The regression rate is the highest near the flame attachment point due to the small distance between the flame and surface. The combustion kinetics plays a significant role in determining the peak regression rate. Furthermore, as U is increased, Da decreases and flame attachment point moves downstream . Therefore, the position of the peaks in regression rate also move downstream of the plate.

As x_l increases beyond the peak shown in Figure 7, the kinetic effects become less significant and transport of heat is the controlling mechanism. As x_l increases, δ increases, the heat feedback qw to the surface and r_0 decrease from their peak values. Furthermore, as the air velocity is increased, convective and conductive transport to the surface increase and r_0 increases significantly as shown in Figure 7. In Figure 7, the area under the curve represents the total mass loss per unit time per unit width of the plate. The area or mass burned increases steadily with x_l and reaches 70% at 3 cm from the leading edge. Clearly, the first few centimeters of the plate contribute significantly to the total mass loss rate and are influenced by different phenomena than at large distances downstream.

3.2 Comparisonof NS with PMMA Experiments for Flame Temperature

Figure 8 shows the steady-state NS solutions for the temperature profiles across the boundary layer flame at different locations along the PMMA plate at U=60 cm/sec. The temperature increases with distance from the surface as one approaches the combustion zone, where most of the energy is released, and decreases as one reaches the bulk of air. Peak temperatures reach near 1900K in the combustion zone. Near the leading edge, the heat release rate due to combustion is high and the peak temperature is high. At large values of x_l, the flame loses heat to the ambient by convection, conduction and radiation as the boundary layers get thick, and the peak temperature decreases with x_l. Figure 8 also shows that the width of temperature peaks increases as the flame thickness increases with x_l due to reduced reaction-diffusion rates. Figure 8 also shows experimental data for temperature with distance from the surface y and at different distances from the leading edge x_l. The temperature data were obtained about 1 min after ignition. Figure 8 suggests that the temperature profiles reached steady-state quickly, within 1 min. Clearly, Figure 8 shows excellent agreement between the predicted peak temperatures and the data. At large distances from the leading edge, the NS solutions seem to over-predict the temperatures on the fuel side of the flame in the region between the combustion

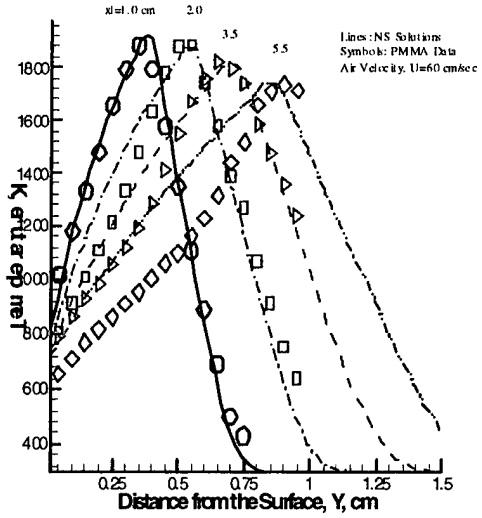

Figure 8 Comparision of NS solutions and PMMA Experiments for Temperature Profiles at Different Distances xL from the Leading Edge of the Fuel Plate

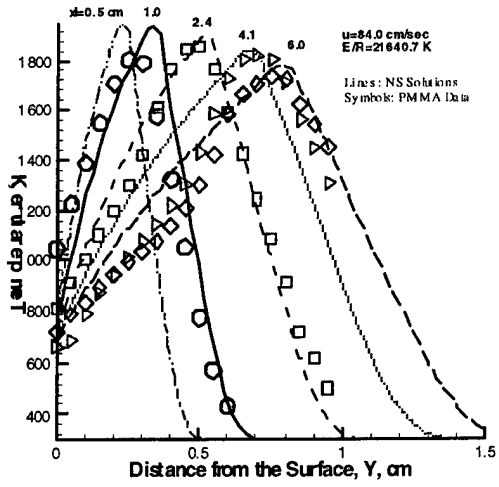

Figure 9 Comparision of NS solutions and PMMA Experiments for Temperature Profiles different values of xl and at U=84 cm/sec

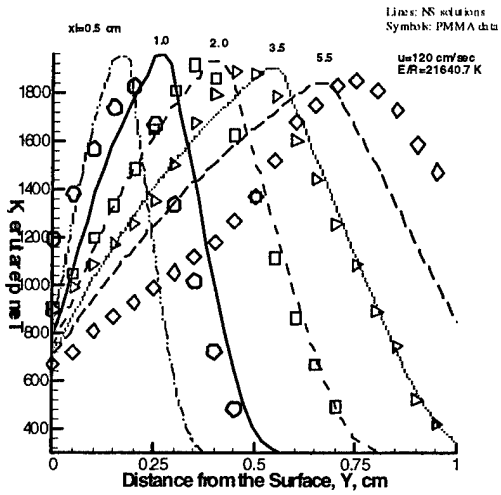

Figure 10 Comparision of NS solutions and PMMA Experiments for Temperature Profiles different values of xl and at U=120 cm/sec

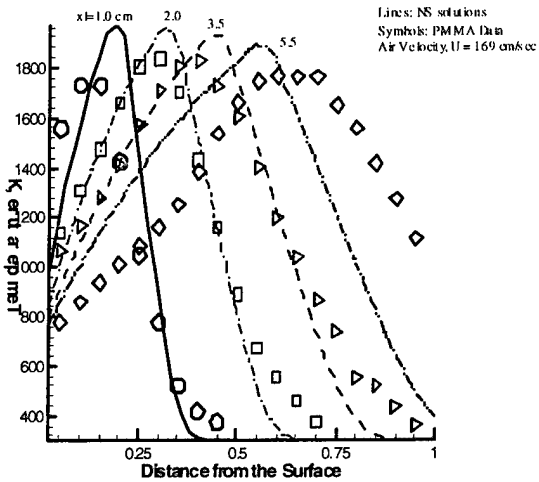

Figure 11 Comparision of Theoretical Temperature Distributions with PMMA Data for Air Velocity, u=169 cm/sec

BEST AVAILABLE COPY

zone and the surface. In the experiments, there is significant soot formation, as indicated by the brightness of the flame. The soot concentration is expected to be high on the fuel side of the flame and increase with distance from the leading edge due to increased MMA concentration. The soot enhances radiative loss from the flame and, perhaps, explains the slight discrepancy between the data and the computations at large values of x_l.

Figures 9 to 11 show temperature profiles at increased values of U. As U increases, the flame-to-surface distance δ decreases and the gradients increase. Figures 9 to 11 show reasonably good agreement between the numerical predictions and the data at the increased values of U. At large values of U=169 cm/sec, the model appears slightly (about 1 mm) to under-predict the position of the temperature peak and over-predict the peak value at large values of x_l. In the experiments, the flame was observed to flicker slightly at large x_l and may lead to lower peak temperatures. Furthermore, y=0 represents the surface of unburnt sample. In the experiments, the surface, however, regresses and the measured temperatures are much higher than the predictions at y=0, especially at small values of x_l, as one might expect.

The flame is located at the peaks of the temperature profiles shown in Figures 8 to 11. In boundary layer flames, the flame-to-surface distance δ increases with x_l and decreases with U as indicated by the positions of the peaks in Figures 8-11. The classical boundary layer solutions for the non-dimensional δ/x_l given by equation (15), NS solutions and the experimental data are plotted together in Figure 12. The NS solutions are given by equation (11). Clearly, NS solutions and the data show that δ/x_l varies both with Re and air velocity U, unlike the classical boundary layer solution, which contains a single parameter Re. The NS solutions consider finite rate combustion kinetics and exhibit a maximum at small values of Re before approaching zero as Re approaches zero. The curves for U= 60 and 84 cm/sec also exhibit peaks, which are outside the scale shown in Figure 12. As expected, the classical BL solutions approach infinity as Re approaches zero due to flame sheet assumptions. Furthermore, at a fixed value of Re, δ/x_l decreases with increased U for small values of $Re^{1/2}$. As U increases, the "flame attachment point" moves downstream and x_l increases at the attachment point. Therefore, the peak value of δ/x_l at the attachment point decreases, and δ/x_l varies both with Re and U. As x_l and Re

BEST AVAILABLE COPY

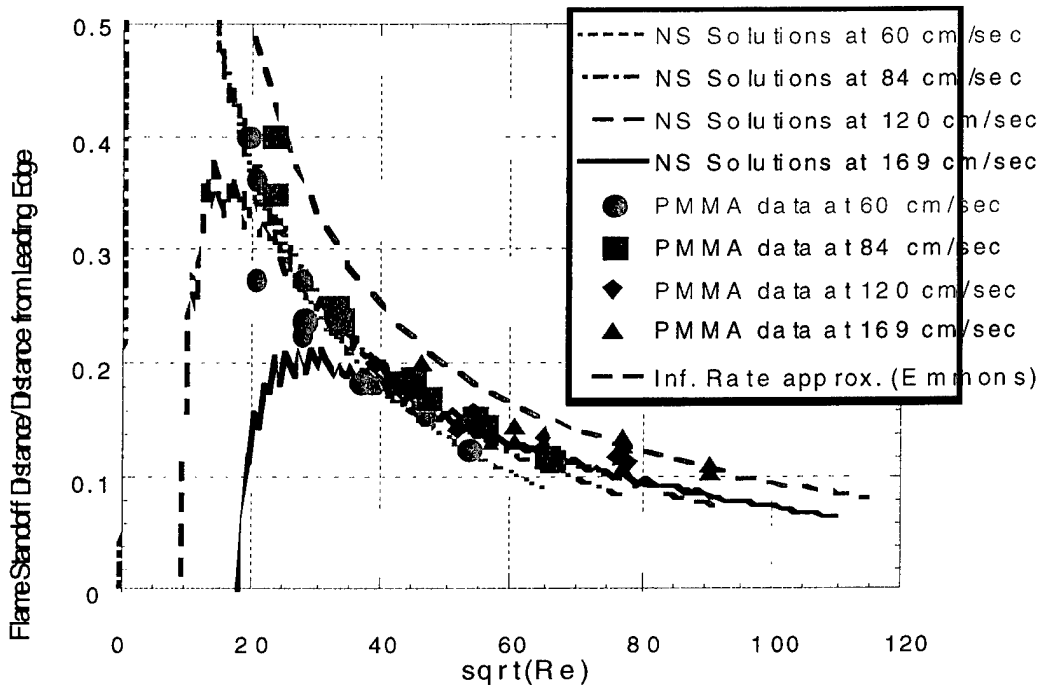

Figure 12 Comparision of NS Solutions for Flame Standoff Distance with PMMA data and the Classical Boundary Layer (BL) Theory Given by 10.0/sqrt(Re)

Re increase, the NS solutions run parallel to the classical solutions and δ/x_l appear to depend only on Re. Furthermore, the NS solutions for δ/x_l remain lower than the classical solutions. As x_l and Re increase further approaching the post flame plate, the NS solutions deviate from the classical solutions due to the lack of transpiration cooling on the inert plate. More significantly, the NS solutions for δ/x_l are in good agreement with the PMMA data for different values of Re and U.

3.3 Comparison of NS with Emmons Theory for Burning Rates

Figures 13 to 16 show the dimensionless regression rate Nu predicted by the NS solutions given by equation (11) at different values of U along with the classical theory of Emmons given

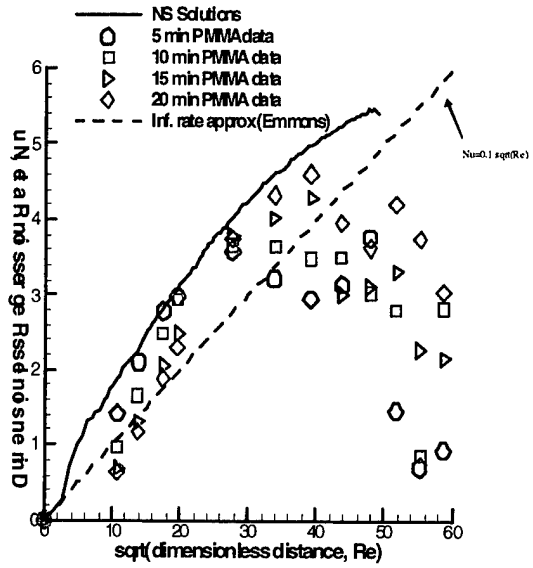

Figure 13 Comparision of Steady State NS Solutions and BL theory with PMMA Experiments Performed for Different Burn Times and at Fixed U=60 cm/sec

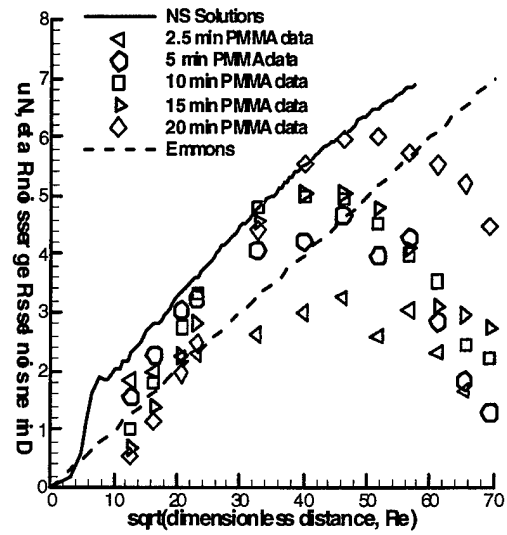

Figure 14 Comparision of Steady State NS Solutions and BL theory with PMMA Experiments Performed for Different Burn Times and at Fixed U=84 cm/sec

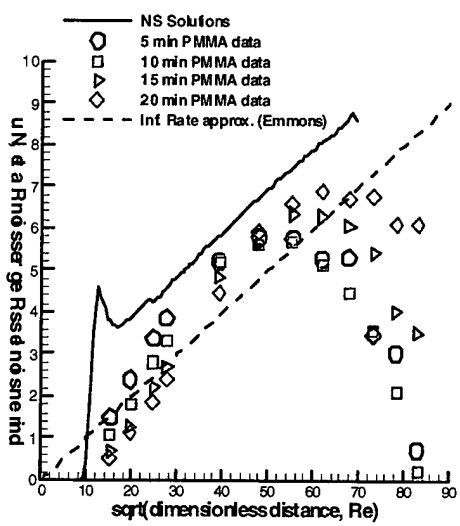

Figure 15 Comparision of Steady State NS Solutions and BL theory with PMMA Experiments Performed for Different Burn Times and at Fixed U=120 cm/sec

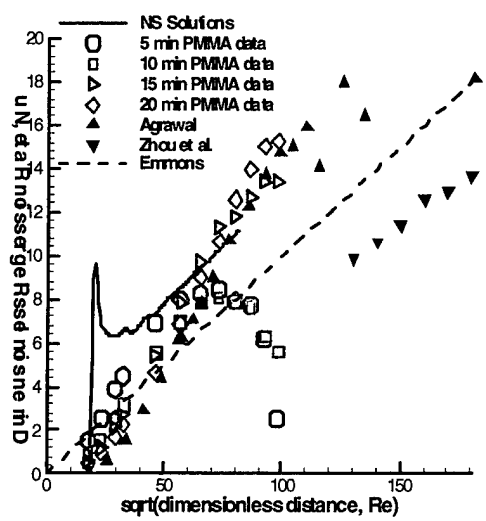

Figure 16 Comparision of Steady State NS Solutions and BL theory with PMMA Experiments Performed for Different Burn Times and at Fixed U=168 cm/sec

BEST AVAILABLE COPY

by equation (14). Both the NS solutions and the classical solutions show that Nu increases with Re as the convective transport of heat from the flame to the surface increases. However, at low air velocities, U=60 and 84 cm/sec, the increase in the value of Nu predicted by the NS solutions do not follow the square-root law unlike Emmons solutions for $Re^{1/2}$ <60. As the air velocity U is increased, the NS solutions appear to follow a square-root law as indicated by the dark, solid, relatively straight lines in Figures 15 and 16 even at relatively low values of $Re^{1/2}$ >30. Therefore, Figures 13 to 16 show that Nu predicted by NS solutions contain two independent parameters Re and U, unlike the classical solutions. As U and Re are increased, the axial diffusion terms become smaller and the NS solutions approach the classical boundary layer solutions qualitatively. Quantitatively, however, NS predictions are higher than Emmons solutions. For example at U=168 cm/sec, $Re^{1/2}$= 80, NS solutions predict Nu=11 vs 6.4 (~40%) as given by the classical boundary layer theory. Indeed for U>120 cm/sec, the NS solutions may be represented by

$$Nu = \varepsilon + 0.1\,\mathrm{Re}^{1/2} \qquad (16)$$

for $Re^{1/2}$>30. The slope in equation (16) is found to be identical to that in equation (14). Here, the non-zero intercept "ε" depends on the burning rate near the flame attachment point, which depends on the competition between convection and reaction rates represented by Da. Indeed, one can obtain the value of ε by fitting equation (16) to Figures 14 to 16. The intercept increases with U; ε=1.5 @ U=84, ε=2.0 @ U=120.0, ε=2.8 @ U=168 cm/sec. This may suggest that ε is inversely proportional to Da.

Clearly Nu predicted by NS solutions are higher than classical BL theory due to various approximations discussed above. This is qualitatively consistent with the calculations of Chen and Tien [6], who showed that the NS solutions very close to the leading edge ($Re^{1/2}$<30) are slightly higher than Emmons as shown in their Figure 11.

3.4 Comparison of NS with PMMA Experiments for Burning Rates

Figures 13 to 16 also show experimental measurements for the regression rates at different values of the burn times. In these experiments, the entire sample is burned for a prespecified time t, which was varied from 5 to 20 min. Clearly, the measured burning rates vary with t significantly unlike the theories which assume steady state. Since the temperature measurements shown in Figure 8 suggest that the transport processes in the gas phase are at

steady state, the long transient exhibited by the data in Figures 13 to 16 must stem from the unsteady phenomena in the condensed phase. Unlike the gas phase transport, which occurs rapidly on a short time scale, transport in the condensed phase is slow due to high thermal mass and occurs over long time scales exhibited by the data in Figure 13-16. There are two kinds of

transient phenomena that have opposite effects on Nu; (1) moving boundary or curvature effect at small values of x_l or Re; and (2) in-depth pyrolysis effect at large values of x_l or Re.

3.5 Moving Boundary Effects

At small values of x_l or Re, Figure 13 shows that the measured Nu at t=5 min are slightly below the NS predictions. As time progresses, the deviations between the NS solutions and the data increase. The steady-state NS solutions and Emmons theory assume that the solid surface remains flat as it burns. In the experiments, however, the initially flat surface becomes curved as it regresses and is shown in Figure 17. Figure 17 shows the formation of a valley or a step near the flame "attachment" point as time progresses and is discussed by Ndubizu et al. [16,17,33-35] in detail. In the boundary layer configuration, the surface regression is non-uniform due to the variation in heat feedback and r_0, which was shown in Figure 8. Figure 17 shows that the surface curvature increases as one approaches the valley from the leading edge of the plate and then decreases with x_l as the heat feedback decreases. The variation in the curvature can result in the formation of a relatively stagnant region behind the step. Due to the increased barrier for diffusion and increased surface area, the concentration of monomer vapor can be higher and that of oxygen lower in the valley than on the flat portion of the surface. This can lead to increased flame stand-off distance, which was observed from the measurements of temperature profile across the valley made in the experiments. Due to the high molecular weight, horizontal geometry, short length of the fuel plate and thin and viscous melt, very little melt flow was noticed across the entire length of the plate in the experiments. The flame standoff distance increases with time as the valley deepens and widens as shown by the surface profiles in Figure 17. The increased size of the valley causes the local regression rate r_0 at the valley to decrease with time as discussed in detail by Ndubizu et al. [16,17]. Therefore, the data for Nu shown in Figure 13 decrease with time unlike the steady-state theories at small values of x_l or Re. At large values of x_l or Re, the surface is relatively flat as shown in Figure 17, and the moving boundary effects on Nu are negligible.

At t=5 min and small values of Re, the circles shown in Figure 13 are close to the NS solutions, since the deviation from the flat surface assumption are small as shown by Figure 17. Figure 17 also shows that the shape of the solid surface deviates from being flat to an increasing distance from the leading edge x_l, as time progresses. Therefore, the deviations between the measured and predicted values of Nu extend to increasing distance x_l or Re with time in Figure 13. The moving boundary effects extend to about $Re^{1/2}$= 14 (or x_l=0.5 cm) at t=5 min and $Re^{1/2}$= 28 (x_l=2.0 cm) at t=20 min as indicated by the deviation between the data (circles, diamonds) and NS solutions for Nu. Indeed, Figure 13 shows the spread rate of the moving boundary effects with time.

As the air velocity is increased, the heat transfer to the surface increases at a given value of x_l due to increased flame attachment distance and decreased flame standoff distance in both the experiments and theory. Therefore, increased air velocity leads to increased deviation from the flat surface at a fixed burn time due to the increased heat transfer. This leads to increased deviation between the data and predictions of NS solutions with the increased U as shown in

Figures 14-16 at fixed values of the burn time and x_l. For example, at x_l=2.0 cm, Figure 13 shows little deviation between data and NS solutions at U=60 cm/sec ($Re^{1/2}$= 28). On the other hand, Figure 16 shows significant deviation at x_l=2 cm and U=168 cm/sec ($Re^{1/2}$= 46). Figures 14-16 also show that the moving boundary or the curvature effects on Nu spread to increased values of Re with increased U, at a fixed value of t. For example, at t= 20 min, Figure 16 shows that the moving boundary effects extend to $Re^{1/2}$= 65 (x_l=4 cm) at U=168 cm/sec compared to $Re^{1/2}$= 28 (x_l=2 cm) at U=60 cm/sec shown in Figure 13.

At large air velocities, 168 cm/sec, both NS solutions and experiments show that the flame attaches ~ 3 mm downstream of the leading edge of the plate. Within the quench distance, spontaneous combustion could not be sustained. After the valley or step was formed in the experiments, it was found that the flame and the valley spread upstream very slowly toward the leading edge of the PMMA plate, and the valley gets wider as the time progresses [31,34,35]. It appears that the valley stabilizes the flame and enables it to spread upstream across the quench distance. As the flame spreads upstream, a fixed point on the surface is exposed to decreasing heat flux, which can result in decreased regression rate with time. However, the upstream spreading is very slow and is expected to have a relatively small effect on r_0 compared to the effects of increasing curvature with time.

3.6 In-Depth Pyrolysis

At large values of x_l or Re, Figures 13 to 16 show that the measured values of Nu increase with the increased burn time, and approach the NS solutions at large values of the burn time. This is opposite to the effects of moving boundary, which occur at small values of x_l or Re, on Nu. The NS solutions assume that the pyrolysis reaction occurs at the surface rather than in the bulk of the polymer melt. Since the surface has no volume, it reaches steady state instantly, and all of the heat flux arriving at the surface is expended in unzipping the polymer as described by equation (5). In the experiments, however, the heat is conducted into the bulk of the solid, which takes a significant time to melt and heat up. As the thermal boundary layer gets thicker, pyrolysis occurs at the surface and in the bulk. Therefore, only a part of the heat flux arriving at the surface is used to unzip the polymer in the experiments at any given time. Experiments [3,10,11], which were performed by exposing a PMMA plate to a uniform radiant flux without combustion, showed that the pyrolysis rate increases with time before reaching a steady-state. The transient period increases from less than 5 min at 5 W/cm^2 flux to 20 min at 1.6 W/cm^{2}as shown in Figure 3 of Reference [3]. We calculate the surface heat flux from Figure 8 using equation (9). The surface heat flux was found to vary from 3.2 W/cm^2 at x_l=0.4 cm to 0.6 W/cm^2 at x_l=6.5 cm for the conditions shown in Figure 14 in the present study. We expect that the transient time for heat up to be significantly small in the present study since the surface was melted and prepyrolyzed prior to ignition. Therefore, the leading edge region exhibits unsteady pyrolysis due to the moving boundary effects rather than due to transient heat up in the present study. As x_l or Re increases, Figure 13 shows that it takes a longer time for the pyrolysis rate Nu to reach steady state due to the in-depth pyrolysis. For example, at $Re^{1/2}$ = 34 (x_l= 3 cm), Nu reached its steady-state value within 20 min as indicated by the small deviation from the NS solution at U=60 cm/sec in Figure 13. However, at $Re^{1/2}$= 50 (x_l= 6.5 cm), Figure 13 shows

unsteady state in the data, which are significantly lower than the NS solution within the same time period.

Figure 13 also shows that the steady-state, surface-pyrolysis approximation is valid for the middle region of the PMMA plate. For example, the data represented by the circles are close to the NS solutions between $Re^{1/2} = 14$ ($x_l = 0.5$ cm) and $Re^{1/2} = 28$ ($x_l = 2$ cm) at t=5 min. Below $x_l < 0.5$ cm, moving boundary effects are significant and above $x_l > 2$ cm, in-depth pyrolysis effects are significant. As time progresses, both the moving boundary effects and the steady-state pyrolysis front spread downstream. The data represented by the red diamonds are close to the NS solutions between $Re^{1/2} = 28$ ($x_l = 2$ cm) and $Re^{1/2} = 34$ ($x_l = 3$ cm) at t=20 min. Thus, Figure 13 shows the spread rates of the moving boundary and steady-state pyrolysis fronts, which are an order of magnitude lower than the traditional co-current flame spread measurements made at the polymer surface [42]. The spreading of both the fronts is controlled by the transport in the condensed phase rather than the gas phase transport.

As the air velocity U is increased, the heat flux to the surface qw increases due to the decreased δ at any given x_l. Therefore, pyrolysis reaches steady state faster than at low velocities as shown in Figures 13-16 at a fixed value of x_l. At U=60 cm/sec, Figure 14 shows that steady-state was not reached at x_l=6.0 cm ($Re^{1/2} = 48$) in 20 min as indicated by the deviation between the red diamonds and the NS solutions. At U=168 cm/sec, however, Figure 16 shows that steady state was reached within the 20 min at x_l=6.0 cm ($Re^{1/2} = 80$). Figures 13 to 16 also show that the steady state pyrolysis front spreads to increased distance x_l with increased U like the spread of the moving boundary effects. For example, at U=168 cm/sec, Figure 16 shows that the steady-state, surface-pyrolysis approximation is valid between x_l=4 cm ($Re^{1/2} = 65$) and x_l=9.5 cm ($Re^{1/2} = 100$) at t=20 min. On the other hand, at U=60 cm/sec, the steady state pyrolysis approximation is valid between x_l=2 and 3 cm at t=20 min.

The increase in Nu at a fixed value of x_l in our experiments is expected to be different in magnitude from the flame less pyrolysis studies [10,11] and from the co-current flame spread studies due to differences in the initial conditions. In the flame spread [12,13,15] and flameless pyrolysis studies [10,11], the sample was at room temperature at t=0 unlike in the present study, where the surface was prepyrolysed under a radiant panel prior to the formation of the boundary layer flame. Therefore, the surface layer was melted and reaches steady state quickly similar to the study of Krishnamurthy and Williams [2].

3.7 Comparisonsof NS with Literature Data

Very few studies reported regression rate data for the forced convection boundary layer flame on a PMMA plate in the literature. The data were often derived from co-current flame spread experiments in which burn time were not clearly defined due to differences in ignition procedure. Therefore, it is difficult to make quantitative comparisons among the data and the theories. However, qualitative trends may be observed by making comparisons between the current study and the previous data.

Agrawal [15] performed experiments on co-current flame spread underneath a horizontal PMMA plate, which was fixed to the ceiling of a rectangular channel. Air was forced through the channel at a prespecified velocity. The plate was ignited by a pilot flame (3 cm long) near the leading edge and was allowed to spread to the end of a 76 cm long PMMA (white) plate. Agrawal [15] measured the surface regression at different values of x_l at the end of the flame spread experiment. Agrawal [15] calculated the values of the surface heat flux from the measured values of regression and the time using the theory given by Agrawal and Atreya [3] for the unsteady conduction heat transfer into the solid. Agrawal and Atreya [3] derived analytical expression for regression rate as a function of time for specified values of the surface heat flux. The surface heat flux was assumed to be independent of time since the gas phase transport reaches steady state very quickly. Agrawal [15] calculated the values of the surface heat flux by substituting the measured values of regression and the time into the analytical expression derived by Agrawal and Atreya [3]. Thus, Agrawal [15] reported the steady state values of the surface flux profile along the PMMA surface for distances between 0 and 40 cm. The surface flux profiles exhibited peaks with x_l and were found to be significantly different from Emmons solutions. At large values of x_l, however, the surface flux profiles shown in their Figure 2 in reference [15] seem to become roughly parallel to the line representing a square-root relationship predicted by Emmons.

The surface heat flux distribution reported by Agrawal [15] are non-dimensionalized using equation (11) to obtain values of Nu and are plotted in Figure 16. The NS solutions do not extend to large distances unlike Agrawal's [15] experiments. However, Figure 16 appears to show reasonably good agreement among the NS solutions (when extrapolated), our experimental data for PMMA for large burn time, and Agrawal's [15] data for $80<Re^{1/2} < 140$ ($x_l > 6$ cm). Both the NS solutions and the data appear to show square-root relationship between Nu and Re for $x_l>6$ cm. For $x_l<6$ cm ($Re^{1/2} < 80$), Agrawal's [15] data are well below the NS predictions like the data obtained by Ndubizu et al. [17] at large burn time due to the moving boundary effects. In Agrawal's experiments, the first few centimeters of the plate might have developed a large valley quickly due to the large over-hang (3 cm) of the pilot flame during ignition, and led to large moving boundary effect on Nu.

Zhou and Fernandez-Pello [13] conducted experiments on co-current flame spread over a long PMMA plate fixed to the floor of a rectangular channel. Zhou and Fernandez-Pello [13] reported values of Nu for 15 cm$<x_l<$70 cm and performed the experiments for a period of 20 min. Therefore, any given point on the surface burned for 20 min or less during the flame spread process. Since no measurements were reported for the first 15 cm of the plate, one might expect little effect due to the moving boundary. Figure 16 compares the NS solutions with a correlation of the data reported by Zhou and Fernandez-Pello [13] for $Re^{1/2} > 125$. We rescaled the correlation given originally by Zhou and Fernandez-Pello [13] to $Nu=0.076\ Re^{1/2}$ based on the values of the constants $\lambda w = 0.052$ W/mK and $\Delta T=1200$ K used in the present study as shown in Figure 16. Figure 16 shows that the data of Zhou and Fernandez-Pello [13] is lower than the steady-state NS solutions perhaps due to significant in-depth heat transport at large values of x_l. Unlike the NS solutions, the correlation of the data given by Zhou and Fernandez-Pello [13] seem to suggest that Nu depends only on Re. However, a closer look at their data given in Figure

5 of reference [13] shows a slight downward deviation from the correlation for Nu at large values of x_1 and could be due to large effects of in-depth pyrolysis.

Krishnamurthy and Williams [2] formed forced convection boundary layer flames on a PMMA plate (15 cm) by igniting the entire surface at once rather than by flame spread. However, they conducted the experiments for a very short period (~100 sec) of time. Krishnamurthy and Williams [2] showed a square-root relationship between the measured regression rates and x_1 at high oxygen concentrations, where the heat flux to the surface might be high and in-depth pyrolysis might occur relatively quickly. At atmospheric concentration of oxygen, however, their regression rate data are much lower than Emmons theory and are similar to the data presented in this work as shown in Figure 16. In ambient oxygen, the surface heat flux is significantly small and leads to large transient effects due to in-depth pyrolysis.

4.0 CONCLUSIONS

Solutions of NS equations show that Nu depends both on Re and U. At large Re and U, the solutions approach the square-root law given by the classical Emmons solutions. Therefore, the boundary layer approximations significantly affect Nu for $Re^{1/2} < 120$ considered in this work. Unlike the theories, PMMA experiments show that Nu depend on Re, U and burn time t. Comparisons of NS solutions with the experiments show that the steady-state surface pyrolysis approximation is valid upstream of the plate at short burn times when the deviations from the flat surface are small. At short burn times, the transient effects due to in-depth pyrolysis become increasingly significant at increased values of x_1 and the NS solutions over-predict the data. As the burn time is increased, the NS solutions over-predict the data near the leading edge due to increased surface curvature. On the other hand, the measured values of Nu increase at large values of x_1 and approach NS solutions at steady state. As the air velocity is increased, the transient moving boundary effects increase and the effects of transient in-depth pyrolysis decrease at a given value of the burn time. Therefore, the deviations between NS solutions and the data for Nu increase upstream and decrease downstream as U is increased. When the time effects are taken into consideration, both the NS solutions and the experiments appear to be qualitatively consistent with data reported by Agrawal [15], Zhou and Fernandez-Pello [13] and Krishnamurthy and Williams [2]. Furthermore, the NS solutions for the temperature profiles across the flame are in good agreement with the data for the entire length of the plate.

5.0 ACKNOWLEDGMENTS

We greatly appreciate the advice and help through numerous consultations provided by K. Kailasanath and G. Patnaik of Laboratory for Computational Physics, Code 6410, Naval Research Laboratory, during the development of the FCT based numerical code.

This work was supported by the Office of Naval Research through Naval Research Laboratory and through Code 334, Damage Control Task of FY01 BA2 Surface Ship Technology Program (PE62121N)

6.0 REFERENCES

1. A. Tewarson, SFPE Handbook of Fire Protection Engineering, Second Edition, Chapter 3 (1995)

2. L. Krishnamurthy and F.A. Williams, Fourteenth Symp. (International) on Combust., The Combust. Inst., 1151 (1974)

3. S. Agrawal and A. Atreya, Twenty-Fourth Symposium (International) on Combust., The Combust. Inst., 1685 (1992)

4. H.W. Emmons, Z. Angew Math. Mech., 36, 60 (1956)

5. M. Sibulkin, A.K. Kulkarni, K. Annamalai, Combust. and Flame, 44, 187 (1982)

6. C-H. Chen and J. Tien, Comb. Sci. and Tech., 50, 283 (1986)

7. C.-P. Mao, H. Kodama, and A.C. Fernandez-Pello, Comb. & Flame, 57, 209 (1984)

8. H. Kodama, K. Miyasaka, and A.C. Fernandez-Pello, Combust. Sci. and Tech., 54, 37(1987)

9. S.L. Madorsky, "Thermal Degradation of Organic Polymers", Interscience Publishers, NY (1964)

10. C. Vovelle, J-L. Delfau, M. Reuillon, J. Bransier, and N. Laraqui, Combust. Sci. and Tech., 53, 187 (1987)

11. T. Kashiwagi and T.J. Ohlemiller, Nineteenth Symp. (International) on Combust., The Combust. Inst., 815 (1982)

12. K. Mekki, A. Atreya, S. Agrawal, and I.S. Wichman, Twenty-Third Symp. (International) on Combust., The Combust. Inst., 1701 (1990)

13. L. Zhou and A.C. Fernandez-Pello, Proc. of the Third International Symp. on Fire Safety Sci., 5, 415 (1991)

14. T. Ahmad and G.M. Faeth, Seventeenth Symp. (International) on Combust., The Combust. Inst., 1149 (1978)

15. S. Agrawal, Combust. Sci. and Tech., 91, 187 (1993)

16. C.C. Ndubizu, R. Ananth, P.A. Tatem, "Experimental Investigation of a Forced Flow Boundary Layer Flame Over PMMA", Second Joint Meeting of the US Sections of the Combustion Institute, Oakland, CA, March 26-28, (2001)

17. C.C. Ndubizu, R. Ananth, and P.A. Tatem, "The Burning of a Thermoplastic Material Under a Forced-Flow Boundary Layer Flame", NRL Memo Report, NRL/MR/6180-02-8630, July 31, 2002

18. A. Hegab, T.L. Jackson, J. Buckmaster, and D.S. Stewart, Combust. and Flame, 125, 1055 (2001)

19. C.-P. Mao, A.C. Fernandez-Pello, and P.J. Pagni, J. of Heat Transfer, 106, 305 (1984)

20. K. Seshadri and F.A. Williams, J. Polym. Sci., 16, 1755 (1978)

21. H. Arisawa and T.B. Brill, Comb. & Flame, 109, 415 (1997)

22. T. Kashiwagi, T. Hirata, and J.E. Brown, Macromolecules, 18, 131 (1985)

23. E.S. Oran and J.P. Boris, "Numerical Simulation of Reactive Flow", Elsevier Publishing Co., NY (1987)

24. G. Patnaik, K.J. Laskey, K. Kailasanath, E.S. Oran, and T.A. Brun, "FLIC-A Detailed, Two Dimensional Flame Model", NRL Memorandum Report 6555, Naval Research Laboratory, Washington, DC, September 27, (1989)

25. V. Casulli and D. Greenspan, Int. J. of Numerical Methods in Fluids, 4, 1001 (1984)

26. C.R. DeVore, "Vectorization and Implementation of an Efficient Multigrid Algorithm for the Solution of Elliptic Partial Differential Equations", NRL Memo Report 5504, Naval Research Laboratory, Washington, DC (1984)

27. W.H. Press, B.P. Flannery, S.A. Teukolsky, and W.T. Vetterling, "Numerical Recipes", Cambridge University Press, NY, (1986)

28. Ananth, R., Ndubizu, C.C., Tatem, P.A., "A Numerical Model for the Development of a Boundary Layer Diffusion Flame Over a Porous Flat Plate", NRL Memorandum Report NRL/MR/6183--01-8547, Naval Research Laboratory, Washington, DC, April 23, (2001)

29. R. Ananth, C.C. Ndubizu, P.A. Tatem, G. Patnaik, and K. Kailasanath, Eighth Int. Conf. on Numer. Combust., Society of Indust. and Applied Math. (SIAM), Amelia, FL, March 5-8, (2000)

30. F.A. Williams, "Combustion Theory", 2nd Edition, Addision-Wesley Publishing Co., CA (1985)

31. I. Glassman, "Combustion", 2nd Edition, Academic Press, Inc. FL (1987)

32. A.M. Kanury, "Introd. to Combust. Phenomena", Gordon and Breach Science Pub., NY (1975)

33. C.C. Ndubizu, R. Ananth, and P.A. Tatem, "Stability and Flame Spread Over Poly (Methyl Methacrylate) (PMMA) within the Quenching Distance", NRL Memo Report, NRL/MR/6180-02-8634, August 16, (2002)

34. C.C. Ndubizu, R. Ananth, P.A. Tatem, Halon Options Technical Working Conference, Albuquerque, NM, April 30-May 2, (2002)

35. C.C. Ndubizu, R. Ananth, P.A. Tatem, Technical Meeting of the Eastern States Section of the Combustion Institute, Hilton Head, SC, December 3-5, (2001)

36. R.Ananth, C.C. Ndubizu, P.A. Tatem, G. Patnaik, and K. Kailasanath, Technical Meeting of the Eastern States Section of the Combustion Institute, Hilton Head, SC, December 3-5, (2001)

37. R.Ananth, C.C. Ndubizu, P.A. Tatem, Halon Options Technical Working Conference, Albuquerque, NM, April 30-May 2, (2002)

38. Ananth, R., Ndubizu, C.C., Tatem, P.A., Patnaik, G., and Kailasanath, K., Fall Technical Meeting of the Eastern States Section of the Combustion Institute, Hilton Head, SC, December 2-5, (2001)

39. Ananth, R., Ndubizu, C.C., Tatem, P.A., Patnaik, G., and Kailasanath, K., The Second Joint Meeting of the U.S. Sections of the Combustion Institute, Oakland, CA, March 26-28, (2001)

40. Ananth, R., Ndubizu, C.C., Tatem, P.A., Patnaik, G., and Kailasanath, K, Sixth International Microgravity Combustion Workshop, Cleveland, OH, May 22-24, (2001)

41. Ananth, R., Ndubizu, C.C., Tatem, P.A., Patnaik, G., and Kailasanath, K, Halon Options Technical Working Conference, Albuquerque, NM, April 24-26, (2001)

42. A.C. Fernandez-Pello, Combust. and Flame, 36, 63 (1979)

APPENDIX A – CONSERVATION EQUATIONS

Continuity

$$\frac{\partial \rho}{\partial t} + \frac{\partial \rho u}{\partial x} + \frac{\partial \rho v}{\partial y} = 0 \ , \qquad \text{(A1)}$$

x-momentum

$$\frac{\partial u}{\partial t} + \frac{\partial \rho u^2}{\partial x} + \frac{\partial \rho u v}{\partial y} = -\frac{\partial P}{\partial x} + \frac{\partial \tau_{xx}}{\partial x} + \frac{\partial \tau_{yx}}{\partial y} \ , \qquad \text{(A2)}$$

y-momentum

$$\frac{\partial v}{\partial t} + \frac{\partial \rho u v}{\partial x} + \frac{\partial \rho v^2}{\partial y} = -\frac{\partial P}{\partial y} + \frac{\partial \tau_{xy}}{\partial x} + \frac{\partial \tau_{yy}}{\partial y} \ , \qquad \text{(A3)}$$

energy

$$\frac{\partial E}{\partial t} + \frac{\partial u(E+P)}{\partial x} + \frac{\partial v(E+P)}{\partial y} = \frac{\partial u \tau_{xx}}{\partial x} + \frac{\partial u \tau_{xy}}{\partial y} + \frac{\partial v \tau_{yx}}{\partial x} + \frac{\partial v \tau_{yy}}{\partial y}$$
$$+ \frac{\partial q_x}{\partial x} + \frac{\partial q_y}{\partial y} + \frac{W_k \Delta H_c}{Av} + Q_r \ , \qquad \text{(A4)}$$

specie,k, conservation

$$\frac{\partial C_k}{\partial t} + \frac{\partial u C_k}{\partial x} + \frac{\partial v C_k}{\partial y} = \frac{\partial U_{dk} C_k}{\partial x} + \frac{\partial V_{dk} C_k}{\partial y} + W_k \ , \qquad \text{(A5)}$$

where ρ is the gas density. The quantities u and v are axial and vertical velocity components in x and y directions respectively. Here, P is pressure, E is total energy density and C_k are specie number densities.

A.1 Transport Fluxes

The viscosity μ effects are contained in shear stress τ, which relates to velocity gradients by the following equations,

$$\tau_{xx} = \mu_m \left(\frac{4}{3}\frac{\partial u}{\partial x} - \frac{2}{3}\frac{\partial v}{\partial y} \right), \qquad \text{(A6)}$$

$$\tau_{xy} = \tau_{yx} = \mu_m \left(\frac{\partial u}{\partial y} + \frac{\partial v}{\partial x} \right), \qquad \text{(A7)}$$

and

$$\tau_{yy} = \mu_m \left(\frac{4}{3}\frac{\partial v}{\partial y} - \frac{2}{3}\frac{\partial u}{\partial x} \right). \qquad \text{(A8)}$$

The conductive fluxes q depend on gas conductivity λ and temperature gradients and are given by

$$q_x = -\lambda_m \frac{\partial T}{\partial x} + \sum_{k=1}^{N} (h_k C_k U_{dk}) / Av \qquad \text{(A9)}$$

and

$$q_y = -\lambda_m \frac{\partial T}{\partial y} + \sum_{k=1}^{N} (h_k C_k V_{dk}) / Av . \qquad \text{(A10)}$$

The first term in equations (A9) and (A10) represent thermal conduction , the second term represents Defour effects, where h_k is specific enthalpy of specie k, Av is Avagadro number, λ is gas conductivity and T is gas temperature. The diffusive fluxes in x and y directions are U_{dk} and V_{dk}, respectively, and are given by

$$U_{dk} = -\frac{1}{X_k} D_{km} \frac{\partial X_k}{\partial x} + \sum_{k=1}^{N} \frac{Y_k}{X_k} D_{km} \frac{\partial X_k}{\partial x}, \; k = 1,2,\ldots N, \qquad \text{(A11)}$$

and

$$V_{dk} = -\frac{1}{X_k} D_{km} \frac{\partial X_k}{\partial y} + \sum_{k=1}^{N} \frac{Y_k}{X_k} D_{km} \frac{\partial X_k}{\partial y}, \; k = 1,2,\ldots N, \qquad \text{(A12)}$$

where, X_k and Y_k are mole and mass fractions of specie k respectively, and D_{km} are equivalent binary diffusivities of specie k in the gas mixture. The gas mixture contains N number of components.

A.2 Thermodynamic Equations of State

Equations of state further define the total energy density E, specific internal energy e and specific enthalpy h_k as

$$E = \rho e + \frac{1}{2}\rho(u^2 + v^2)\,, \qquad \text{(A13)}$$

$$\rho e = \sum_{k=1}^{N} \frac{C_k h_k}{Av} - P\,, \qquad \text{(A14)}$$

and

$$h_k = a1_k + a2_k T + a3_k T^2 + a4_k T^3,\ \mathrm{k} = 1,2,\ldots \mathrm{N}\,, \qquad \text{(A15)}$$

where $a1_k$...,$a4_k$ are polynomial coefficients for specie k and are taken from sources such as those compiled by NIST (www.nist.gov), University of Berkeley (www.ucb.edu) as discussed by Ananth etal. [28]. The ideal gas law is

$$P = RT\sum_{k=1}^{N}\frac{C_k}{Av}\,, \qquad \text{(A16)}$$

the mass specific heats C_{pk} of specie k are

$$C_{pk} = \frac{1}{M_k}\frac{\partial h_k}{\partial T},\ \mathrm{k} = 1,2,\ldots \mathrm{N}\,, \qquad \text{(A17)}$$

and the mass specific heat of the gas mixture C_{pm} is

$$C_{pm} = \sum_{k=1}^{N} Y_k C_{pk}\,. \qquad \text{(A18)}$$

A.3 Transport Properties

The transport properties are calculated from kinetic theory of gases described by Chapman-Enskog equations. The diffusivities of specie k in a mixture D_{km} are calculated from binary diffusion coefficients D_{ij} and mixture composition using

$$D_{km} = \frac{1 - Y_k}{\sum_{l=1, l \neq k}^{N} \frac{X_l}{D_{kl}}}, \quad k = 1,2,\ldots N, \qquad \text{(A19)}$$

where the binary diffusion coefficients are related to temperature by fitting a power law in the range of 300 to 3000 K to evaluate $b1_{ij}$ and $b2_{ij}$:

$$D_{kl} = b1_{kl} T^{b2_{kl}} / \sum_{k=1}^{N} C_k, \quad k = 1,2,\ldots N. \qquad \text{(A20)}$$

The mixture viscosity is calculated from specie viscosities μ_k and mixture composition Y_k from the following equations

$$\mu_m = \sum_{k=1}^{N} \frac{Y_k \mu_k}{\sum_{j=1}^{N} Y_j \phi_{kj}}, \qquad \text{(A21)}$$

where

$$\phi_{kj} = \frac{1}{\sqrt{8}} \left(1 + \frac{M_k}{M_j}\right)^{-\frac{1}{2}} \left(1 + \left(\frac{\mu_k}{\mu_j}\right)^{\frac{1}{2}} \left(\frac{M_j}{M_k}\right)^{\frac{1}{4}}\right)^2. \qquad \text{(A22)}$$

The specie viscosities are related to temperature by a power law given by

$$\mu_k = c1_k T^{c2_k}, \quad k = 1,2,\ldots N, \qquad \text{(A23)}$$

where $c1_k$ and $c2_k$ are known constants. Mixture conductivities λ_m, which depend on the individual conductivities of the species and mixture composition, are given by

$$\lambda_m = \frac{1}{2} \left(\sum_{k=1}^{N} Y_k \lambda_k + \frac{1}{\sum_{k=1}^{N} \frac{Y_k}{\lambda_k}} \right). \qquad \text{(A24)}$$

The specie conductivities are also related to temperature by a power law

$$\lambda_k = d1_k T^{d2_k}, \quad k = 1,2,\ldots N, \qquad \text{(A25)}$$

where $d1_k$ and $d2_k$, are known constants. Eucken equation is used for the conductivity of H_2O vapor. Therefore, all the transport properties are functions of both the temperature and composition.

A.4 Radiative Loss

Heat loss Q_r from the hot gases to the ambient is assumed to follow Stefan-Boltzman law and is

$$Q_r = K_{pm}\sigma\left(T^4 - T_\infty^4\right). \qquad \text{(A26)}$$

The gray body extinction coefficient, K_{pm}, is calculated based on the concentrations of carbon dioxide and water using

$$K_{pm} = K_{pCO2}Y_{CO_2} + K_{pH2O}Y_{H_2O} \quad , \qquad \text{(A27)}$$

where

$$K_{pk} = K_1 + K_2T + K_3T^2 + K_4T^3 + K_5T^4 + K_6T^5 + K_7T^6 + K_8T^7 \ , \qquad \text{(A28)}$$

subscript k stands for CO_2 or H_2O, and K_1 to K_8 are known constants.

A.5 The BoundaryConditions

The above partial differential equations require specification of boundary conditions on all the dependent variables ρ, u, v, P, E, and C_k at inlet, outlet, upper and lower walls of the channel.

A5.1 At inlet, x=0 and all y values;

The inlet velocity components u_0, total energy E_0,density ρ_0 and composition as number densities C_{k0} are specified. These boundary conditions assume that the inlet is far from the combustion zone so that they are affected by the changes occurring inside the computational domain. The inlet pressure P is unknown. The pressure is expected to change along the channel due to momentum boundary layer development along the channel walls due to friction. However, this pressure change is expected to be small compared to pressure change near the leading edge of the porous plate. Therefore, we specify that the inlet pressure drop to be zero. They are written as

$$u(t,0,y) = u_0, v(t,0,y) = 0, E(t,0,y) = E_0 \ , \qquad \text{(A29)}$$

and

$$\rho(t,0,y) = \rho_0, C_k(t,0,y) = C_{k0}, \frac{dP}{dx}(t,0,y) = 0. \qquad \text{(A30)}$$

A5.2 At outlet, x=L and all values of y;

Again, we assume that the channel outlet is far from the combustion zone so that the outlet conditions are not affected by the changes taking place inside the channel. We set all the gradients to zero. The outlet pressure gradient, however, must be specified to obtain unique solution to the equations. We assume the outlet pressure to be atmospheric. In reality, however, combustion heat is released all the way to the end of the channel, affecting the outlet conditions. But the heat released is less than one tenth of the maximum heat release rate. These approximations are expected to be accurate for high fluid velocities, which exist in forced convection boundary layers. As the inlet velocity decreases, they become less accurate and the solutions near the end of the channel (1-2 cm near exit) are not accurate. The boundary conditions are written as

$$\frac{du}{dx} = \frac{dv}{dx} = \frac{dE}{dx} = \frac{d\rho}{dx} = \frac{dC_k}{dx}(t, L, y) = 0, \qquad \text{(A31)}$$

and

$$P(t, L, y) = P_{atm}, \qquad \text{(A32)}$$

where $L=L_1+L_2+L_3$.

A5.3 On top solid wall and non-porous sections 1 and 3 of the bottom wall y=H, y=0;

The top wall is assumed to be far enough from the combustion zone so that no heat is transferred to it from the flame. However, there is no slip on the wall and no mass flow through it. They are written as

$$\frac{dE}{dy} = \frac{d\rho}{dy} = \frac{dC_k}{dy} = \frac{dP}{dy}(t, x, H) = 0, \qquad \text{(A33)}$$

and

$$u = v(t, x, H) = 0, \qquad \text{(A34)}$$

for all values of x.

A5.4 At impermeable sections of the bottom wall, y=0

The bottom wall is assumed to conduct heat away from the flame following Newton's law of cooling with a characteristic heat transfer coefficient h. As a result of this boundary condition, the wall will heat up to a temperature T_w, which varies along the wall and is calculated by an iterative method. The adiabatic and constant wall temperature boundary conditions, which were used in the existing works by Mao et al. [7], Kodama et al. [8] and Chen and Tien [6] occur as special cases for h=0 and ∞ respectively. The boundary conditions are written as

$$h_w\left(T(x,0)-T_{atm}\right)=\lambda\frac{dT}{dy}(t,x,0), \qquad \text{(A35)}$$

$$\frac{d\rho}{dy}=\frac{dC_k}{dy}=\frac{dP}{dy}(t,x,0)=0, \qquad \text{(A36)}$$

and

$$u=v(t,x,0)=0, \qquad \text{(A37)}$$

for $x < L_1$ or $x > L_1+L_2$.

A.6 Initial conditions

Initial conditions are taken as the inlet conditions at x=0 over the entire domain. Therefore,

$$u(0,x,y)=u_0,\ v(0,x,y)=0,\ E(0,x,y)=E_0, \qquad \text{(A38)}$$

and

$$\rho(0,x,y)=\rho_0,\ C_k(0,x,y)=C_{k0},\ P(0,x,y)=P_{atm}. \qquad \text{(A39)}$$

Initial conditions are applied prior to ignition.

BEST AVAILABLE COPY